Additive Manufacturing 50 (2022) 102540

Contents lists available at ScienceDirect

Additive Manufacturing

journal homepage: www.elsevier.com/locate/addma

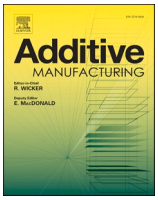

On the detailed morphological and chemical evolution of phases during laser powder bed fusion and common post-processing heat treatments of IN718

Vitor Vieira Rielli [a], Alessandro Piglione [b], Minh-Son Pham [b], Sophie Primig [a,*]

[a] School of Materials Science & Engineering, UNSW Sydney, NSW 2052, Australia
[b] Department of Materials, Imperial College London, Exhibition Road, London SW7 2AZ, UK

ARTICLE INFO

Keywords:
Scanning strategy
Precipitates
Atom probe microscopy (APM)
Superalloy
Laves phases

ABSTRACT

IN718 is the most common Ni-based superalloy for manufacturing aircraft engine parts via thermo-mechanical treatments. The evolution of nanoscale strengthening phases is well researched, enabling optimization of strength, fatigue, and creep properties. Recently, IN718 has shown great viability for laser powder bed fusion (LPBF) additive manufacturing of aerospace parts. However, the detailed microstructure-property relationships during thermal profiles typical to LPBF are not yet well understood. Previous works reported interdendritic precipitation of Laves phase. These detrimental particles can be dissolved by heat treatments, however, the detailed nanoscale phase evolution remains unknown. Using atom probe microscopy, we report on the detailed morphological and chemical evolution of phases in IN718 after LPBF with chessboard versus meander scanning strategies, and direct ageing versus homogenization and ageing treatments. Due to differences in scanning vector length, up to 3.6 times larger dendritic structures, double volume fractions of Laves particles, and Al clusters are found in the chessboard strategy. Coarser matrix grains and a higher dislocation density are detected in the meander strategy. The precise chemical composition and morphology evolution of the matrix, Laves, MC, γ', and γ'' phases are obtained and correlated to hardness. Retained Laves phase after direct ageing causes precipitation of 4% volume fraction of γ'', with additional coarsened precipitates formed along dislocations. Direct ageing leads to an increase in hardness corresponding to roughly 190 HV. Due to Laves phase dissolution, a volume fraction of 16% of compositionally stable, larger γ'' precipitates is found after homogenization and ageing, also causing partial matrix recrystallization.

1. Introduction

The aerospace industry has been leading the development of laser powder bed fusion (LPBF) components using materials with well-established supply chains [1–3]. IN718, as the most used Ni-based superalloy, has great potential, and its viability for additively manufactured (AM) parts has been widely demonstrated [3–6]. However, in order to satisfy stringent requirements, significant efforts are still being placed on designing processing parameters and heat treatments to obtain the best combination of high-temperature mechanical properties such as yield strength, fatigue, and creep [7–11].

In LPBF, successive layers of powder are melted by a high energy laser beam. The complex phenomena involved in the solidification, remelting, and reheating of previously deposited layers impact the morphology and chemistry of all phases [12,13]. The formation of dendrites in LPBF occurs due to thermal gradients during non-equilibrium solidification. The constitutional undercooling at the solid-liquid interface is governed by the thermal gradient (G) and the velocity (V) of the solidification interface. High G and low V produces dendritic structures [14,15]. For IN718, low solubility elements such as Nb, Mo, Ti, and C, tend to segregate at the interdendritic regions causing the formation of MC carbides and topologically closed packed (TCP) phases such as the Laves phase $(Ni,Cr,Fe)_2(Nb,Mo,Ti)$ [16]. The latter is brittle and detrimental to mechanical properties with its shape, size, and volume fraction determined by the detailed processing parameters [17]. Higher cooling rates from melting lead to smaller dendrite arm spacings, and consequently reduced potential for formation of the Laves phase [18]. Variations of laser scanning strategy during LPBF have been

* Corresponding author.
E-mail address: s.primig@unsw.edu.au (S. Primig).

https://doi.org/10.1016/j.addma.2021.102540
Received 17 September 2021; Received in revised form 11 November 2021; Accepted 29 November 2021
Available online 1 December 2021

proposed to optimize the microstructures and properties of builds, where islands and meander patterns are commonly used [19,20]. Rotations of 67° or 90° between layers are generally implemented during LPBF, with the latter causing more pronounced epitaxial grain growth along the build direction (BD) [21]. Parameters such as build orientation, laser power, layer thickness, hatch spacing, and scanning speed also affect the microstructure and properties [22–25].

The microstructures of LPBF IN718 parts differ considerably from its conventionally manufactured counterparts [26]. Residual stresses from rapid solidification and thermal cycling lead to a high density of dislocations [27]. In addition to the aforementioned Laves phase and MC carbides, other phases might be formed such as the desirable, nanoscale precipitates γ′ and γ″, δ phase and α-Cr phases [28,29]. Post-processing treatments such as homogenization, solution treatment, and ageing are applied in order to optimize the microstructure and properties. By varying temperature and time, Huang et al. [30] showed the effect of homogenization on the dissolution of the Laves phase, while Zhao et al. [31] investigated the effects of different solution temperatures on δ phase formation. Distinct combinations of these treatments, or the lack of thereof, will affect the solute contents of elements such as Nb and Ti in the matrix, consequently impacting the precipitation of the γ′ (Ni_3(Al, Ti)) and γ″ (Ni_3(Nb)) strengthening precipitates during ageing [32,33]. Analyses of these precipitates following different ageing treatments have been reported recently [17,34–37]. These results are usually obtained by scanning and transmission electron microscopy (SEM/TEM), and small-angle X-ray scattering (SAXS), reporting on the size and volume fraction of γ′ and γ″ precipitates. For γ″, the main strengthening precipitate, sizes from 6 to 64 nm, and volume fractions from 1.7 up to 16.9% have been reported [17,34,37]. This high degree of variability occurs due to chemical redistribution of alloying elements available for precipitation, depending on the detailed LPBF process and post-processing treatments.

The investigation of the detailed evolution of phases is a field yet to be explored in depth in AM of IN718. This is due to small size of the phases and presence of low atomic number elements, representing limitations for techniques such as energy dispersive X-ray spectroscopy (EDS) in SEM or TEM [28,38,39]. Atom probe microscopy (APM) is the only technique able to overcome these issues by allowing precise quantification of elements due to its sub-nanometer resolution [40]. However, only a limited number of publications have used this technique in AM research on superalloys in general, and on IN718 in particular so far. A recent investigation by Mantri et al. [41] presented a detailed analysis of the effects of micro-segregation in the precipitation process in laser surface engineered IN718. Ramakrishna et al. [34] showed the composition of regions across Laves phase in PBF IN718, while Larson et al. [42] explored segregation of elements at grain boundaries. However, a detailed description of the chemical and morphological evolution of phases in IN718 during typical AM processes and post-printing heat treatments is currently unavailable.

Such information is essential for property optimization of AM IN718, and as input data for CALPHAD and thermo-kinetic modelling. In this field, the precipitation kinetics in IN718 manufactured through directed-energy deposited and electron beam melting have been examined by Kumara et al. [43,44], while Zhang et al. [45] presented modelling results of volume fraction of precipitates during thermal exposure at 870 °C in IN625. These computer simulations aim to predict precipitation behavior and consequently the processing and heat treatment parameters that will deliver superior properties.

Thus, the aim of the current study is to reveal the microstructure evolution with particular focus on the chemistry and morphology of nanoscale phases during LPBF and post-printing heat treatments of IN718. To study the influence of the thermal history during printing, two different laser scanning strategies are considered, islands scanning which is similar to a chessboard pattern, and a bi-directional meander pattern. These strategies generate different remelting and cooling rates, and consequently varying fractions of the Laves phase. Selected samples are subjected to direct ageing (DA), and homogenization and ageing (HA). The microstructural evolution and geometrically necessary dislocation (GND) density are revealed via light optical microscopy (LOM), SEM and electron backscatter diffraction (EBSD), respectively. An atomic clustering analysis of the γ matrix in the as-built condition (AB) is achieved via APM. Detailed investigations of the mechanical properties of the same AB materials, such as tensile and fatigue properties, as well as porosity and fracture mechanisms are reported by some of the current authors in [46]. APM is further employed to provide new insights into the morphological and chemical composition evolution during heat treatments. APM results of Laves phase and MC carbides are also presented. Correlation of the micro- and nanostructure with mechanical properties is accomplished through hardness testing. The results have the potential to support current advances in thermo-kinetic modelling and property optimization during LPBF IN718.

2. Materials and methods

IN718 (52.36Ni–18.86Fe–21.19Cr–3.25 Nb–1.87Mo–1.21Ti–1.07Al –0.19 C, at%) gas atomized powder with particle size ranging from 15 to 45 μm was supplied by Höganäs. A Concept Laser M2, operating at a laser power of 225 W, was used to fabricate 140 × 24 × 22 mm^3 bars following chessboard and bidirectional meander laser scanning strategies. As illustrated in Fig. 1a, the former (Chess-AB) consists of 5 × 5 mm^2 randomly scanned meander islands, rotated 90° between each other, with an island overlap of 0.0225 mm. The latter (Meander-AB, Fig. 1e), is a common strategy and has its two opposite scanning vectors represented by the black and white lines. For both strategies, a 90° rotation between each 30 μm thick layer was imposed. For the chessboard strategy, the X and Y island shift between layers was 1 mm. Further parameters were hatch spacing of 60 μm and scanning speed of 2000 mm/s.

As delineated by the white box in Fig. 1a and Fig. 1e, microstructural analyses were carried out at half build height of the YZ face of the cuboidal blocks. Samples were cut, ground, and polished via standard metallography preparation methods [47]. For LOM, samples were etched with Kalling's reagent and images were acquired with a Nikon Eclipse ME600 microscope. For backscatter electron (BSE) imaging, polished samples mounted in conductive resin with carbon filler were imaged in a SEM JEOL 7001 F with accelerating voltage of 20 kV. To determine volume fraction and morphology of Laves phase, for each solidification structure, a 54 μm^2 area was analyzed on ImageJ after smoothing with convolution with a Gaussian function ($\sigma = 1$) and default thresholding of 1–2%. Images were then converted to binary and the area fraction of the Laves phase was determined with the Analyze Particles tool. The size of the dendritic arm spacing (λ) was measured through the line intercept method.

An EDAX 'Hikari Super' system installed in a SEM JEOL 7001 F was used for EBSD, after further polishing samples for 24 h in a VibroMet 2 vibratory polisher on a suspension of MasterMet colloidal silica. EBSD parameters for the grain size study were a camera binning of 6 × 6, map size of 800 × 800 μm^2, and step size of 0.7 μm. For GND analyses, a higher resolution was required, and parameters were changed to camera binning of 4 × 4, map size of 45 × 45 μm^2, and step size of 0.04 μm. The EDAX TSL OIM Analysis 8 software was used for analyses of all maps. For the larger inverse pole figure (IPF) and unique color grain maps, a grain dilation clean-up was executed considering a minimum grain size of 5 points and angle of tolerance of 5 °. For the analysis of grain size, Σ3 and Σ9 twin boundaries were disregarded. For GND maps, the cleaning procedure involved a neighbor orientation correlation clean-up of third level, with a minimum confidence index of 0.1, and tolerance of grain angle of 5°. Following thus, orientation Kernel smoothing was performed for the first iteration, with Kuwahara filter up to the third neighbor, and a misorientation limited to 5°. This GND analysis follows the method developed by Field et al. [48], where GNDs are calculated according to local misorientations. Both edge and screw dislocations,

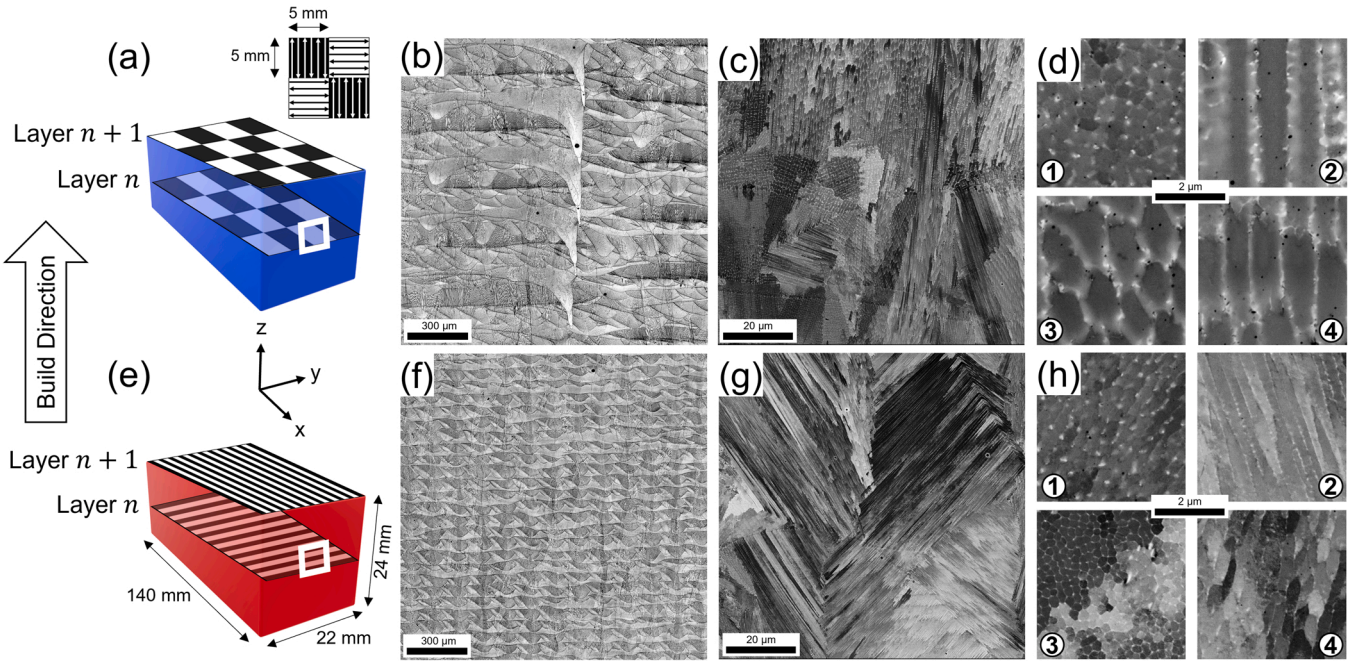

Fig. 1. (a) Illustration of chessboard scanning strategy; images of Chess-AB sample (b) LOM, (c) BSE, (d) solidification structures according to sectioning orientation; (e) illustration of meander scanning strategy; images of Meander-AB sample (f) LOM, (c) BSE, (h) solidification structures according to sectioning orientation. (For interpretation of the references to colour in this figure legend, the reader is referred to the web version of this article.)

and a maximum misorientation of 5° is considered in the GND calculation. Pole figures were obtained through a calculation method of harmonic series expansion, at 16 series rank, and Gaussian smoothing of 5°.

Transmission electron microscopy (TEM) specimens were prepared through twin-jet electropolishing with a Struers TenuPol-5 in 10% perchloric acid solution in methanol at − 5 °C. A JEOL JEM-2100 F operating at 200 kV was used for the TEM observations.

As-built samples were heat treated in an alumina tube-furnace, where DA consists of 9.1 h at 720 °C followed by 50 °C/h furnace cooling to 620 °C, holding for 7.2 h, and subsequential water quenching (WQ). The homogenization procedure was done at 1050 °C for 1 h then WQ followed by the same ageing as described above (HA). Both heat treatments were carried out in a flow rate of 0.2 L/min of Ar. Nomenclature of DA samples are referred to as Chess-DA and Meander-DA, while HA samples are Chess-HA and Meander-HA.

For the nanoscale analysis of the TCP phases, MC carbides, and γ' and γ'' precipitates, APM was used. Tips were electropolished at room temperature in two steps, first a rough polishing at DC voltage of 25 V in 25% perchloric acid in glacial acetic acid, followed by fine polishing at 10–15 V in 2% perchloric acid in 2-butoxyethanol [40]. A CAMECA local electrode atom probe (LEAP) 4000X Si in laser-assisted mode with a detector efficiency of 57% was used. The following parameters were applied for the data acquisition: pulse rate of 200 kHz, laser energy of 50 pJ, and detection rate of 1.0%. An ultra-high vacuum of $< 3.7 \times 10$–11 Torr was maintained in the analysis chamber during the experiment and temperature measured in the channel B was set to 50 K. Data reconstruction was carried out on the AP Suite 6.1 software. Image compression factor and k-factor were set to the standard values of 1.65 and 3.3, respectively. For determining all concentration isovalues that define the phases, a method proposed by Theska et al. [49] was employed, where the differential concentration profiles at the interfaces are used to find the largest concentration gradient. Proximity histograms (proxigrams) with a step size of 0.1 nm were obtained for a total length of 6 nm for MC carbides and 4 nm for Laves phase. Quantitative evaluation of precipitates in DA and HA samples was done using tip volumes of 885,000 ± 2% nm^3. For major axis size, aspect ratio, and oblateness determination, surfaces with volume lower than 10% of the largest precipitate in the dataset were disregarded, as they are considered artifacts due to local variations in the composition. The chemical composition of the phases was determined for all isosurfaces of each respective phase in the datasets. The cluster count analysis was carried out in tip volumes of roughly 60,000 nm^3 containing the γ matrix only, with step size of 0.01 nm, order of 5 ions, and 10 solute ions as the minimum threshold to be confirmed as a cluster.

A Struers DuraScan was used for Vickers hardness testing with 9.8 N force (HV1) observing the ASTM standard E92–82. Ten indents were done to obtain the average value with associated standard deviation.

3. Results

3.1. Microstructure of chessboard and meander samples in the as-built condition

Fig. 1(b-d) and Fig. 1(f-h) show LOM and BSE images of the AB microstructures of Chess-AB and Meander-AB samples, respectively. An evident difference in the arc shaped melt pools is identified in LOM images in Fig. 1b and Fig. 1f. Chess-AB has melt pools with depth varying from 30 to 120 µm, where substantial overlapping is identified [27]. Large keyhole formations as deep as ~350 µm are seen at the intersection of two islands where the scanning directions are rotated 90° [50]. Melt pools in Meander-AB are more homogenous, ranging from 30 to 60 µm in depth, with center-to-center distances matching the hatch spacing of 60 µm. Higher magnifications of melt pool boundary (MPB) regions are shown in Fig. 1c and Fig. 1g. Dendritic structures epitaxially grown across the MPB are present [51]. Different directions of heat extraction in the melt pools during solidification lead to misalignment between the BD and the columnar dendritic structures [52]. This phenomenon is more pronounced in Meander-AB, where regions in between two adjacent melt pools of the same layer tend to grow epitaxially 45° to the BD. Fig. 1d and Fig. 1h display varying solidification structures, whose morphologies depend on the sectioning angle to the growth direction [37,53]. The brighter interdendritic regions are characterized by elements segregated during solidification, which cause the formation of the Laves phase [54–56]. A quantitative evaluation of these structures is

shown in Table 1. The average volume fraction of the Laves phase of 1.92% in Chess-AB is more than two times larger than in Meander-AB (0.88%), and its overall average size is around 130 nm, while in Meander-AB it is 73 nm. For dendritic morphologies of the type 2 and 3 in Chess-AB, the dendritic arm spacing (λ) is 2.8, 3.6 times larger than in Meander-AB, respectively. The morphology of the type 4, similar to a fish-scale, is often formed at the melt pool boundaries [57]. Due to the faint contrast of the interdendritic region in morphology of the type 1, measurement of λ was not carried out in this case.

Fig. 2 shows EBSD images of grains and the corresponding GND mapping of AB samples. Fig. 2a and Fig. 2e illustrate the pole figure representations of the orientation of grains from IPF maps in Fig. 2b and Fig. 2f for Chess-AB and Meander-AB, respectively. For both samples, the pole figures show a preferential grain growth along the BD in the ⟨001⟩ direction, which has been widely reported in the literature [21, 58]. As shown by the multiples of the uniform density (m.u.d) blue-to-red color code bar, Meander-AB shows stronger texture on the ⟨001⟩ direction than Chess-AB. The grain maps in Fig. 2c and Fig. 2g illustrate that grains are elongated along the BD. Supplementary Fig. A1a shows the distribution of grain sizes for both samples and respective fitted curves. Table 1 reveals that the grains in Meander-AB with average size of 44 μm are 25% larger than the 35 μm grains in Chess-AB. The high-resolution GND maps in Fig. 2d and Fig. 2h show that Meander-AB has a denser dislocation network corresponding to 175×10^{12} GND/m^2 in comparison to Chess-AB (153×10^{12} GND/m^2). A mixed quantitative and qualitative approach was followed when analyzing the GND density. On the one hand, large standard deviations are identified since a log-normal data distribution is obtained from the GND analysis, as shown in Supplementary Fig. A1b. On the other hand, fitted curves clearly show different GND density distributions between Chess-AB and Meander-AB.

The microstructure in Meander-AB sample was studied by TEM, to further analyze the dislocation structures as exhibited in Fig. 3. Fig. 3a shows that dislocations are not limited to interdendritic regions, with many entangled dislocations present in the core of the plane view structure whose orientation is determined by the sectioning angle during TEM foil preparation, corresponding to the type 2 solidification structure in Fig. 1h. Fig. 3b shows a transverse cross section of the dendritic substructure, which has most dislocations arranged into its walls, and its diameter of ~300 nm agrees with the values reported for morphology of the type 3 from BSE images (Table 1). The inset SAEDs in Fig. 3(a-b) do not show superlattice reflections, indicating the absence of γ′ and γ″ precipitation during LPBF processing.

3.2. Chemical analysis of MC carbides, Laves phase, and γ matrix in the as-built condition

APM reconstructions of interface regions consisting of interphase boundaries between MC carbides, Laves phase, and γ matrix are displayed in Fig. 4 and Fig. 5. The proxigrams, which show the concentration profile evaluated across all interfacial surface between the phase of interest and the γ matrix determined by the concentration isovalues [40], are also presented in Fig. 4 and Fig. 5. As mentioned in the Materials and Method section, the concentration isovalues were obtained following the enhanced iso-surface method [49]. Supplementary Fig. A2a and Fig. A2c show APM reconstructions of the γ matrix in the dendritic core, i.e., away from other phases, in Chess-AB and Meander-AB, respectively. Table 2 shows the composition of the phases mentioned above. For the γ matrix, on the one hand, slightly larger amounts of the Laves phase forming elements Mo, Cr, and Ti are found in Chess-AB. A 4.18 at% Nb composition, on the other hand, is 10% lower in this condition when compared to a 4.6 at% of Nb in Meander-AB.

The clustering analyses of Al and Nb, the primary forming elements of γ′ and γ″, are presented in Supplementary Fig. A2b and Fig. A2d for Chess-AB and Meander-AB, respectively. The cluster count analyses were carried out on the γ matrix region shown in Fig. A2a and Fig. A2c. It is evident that for Nb, no significant deviation exists between the experimental and randomized count curves for both scanning strategies. The Al experimental curve in Chess-AB slightly deviates from the randomized, indicating that some minor formation of Al clusters might have occurred at the dendritic core during cooling. A similar phenomenon is not observed in Meander-AB. These clusters might impact precipitation during direct ageing, as potential nucleation sites for Al-rich γ′. Some of the author's recent studies on the early stages of precipitation reported similar findings on the influence of Al and Nb clusters during the evolution of precipitates, particularly in the first 0.6 h of DA [59]. Higher temperature treatments, such as homogenization is likely to dissolve these clusters.

The MC carbide in Meander-AB shown in Fig. 4a has an irregular shape. The proxigram in Fig. 4b shows that a depletion in Ni, Cr, and Fe is observed across the MC carbide/γ matrix interface. Nb, Ti, Mo, and C display opposite trend. Table 2 confirms an enrichment of Nb (31.71 at %) and Ti (11.69 at%) in the carbide, at proportions of 0.8 and 0.3 when related to C (38.68 at%). Ni, Mo, and Cr are also present in much smaller fractions.

The Laves phase in Chess-AB shown in Fig. 5a contains amounts of Nb (19.77 at%) and Mo (4.64 at%) exceeding several times the amount found in the matrix, and lower amounts of Ni, Fe, and Cr. The proxigram in Fig. 5b shows that across the interphase boundary, there is an increase in Nb and Mo and decrease of Ni and Al. Variations in Cr and Fe concentrations are small, while Ti seems to segregate to the interface. Table 2 shows that the Laves phase is mostly composed of Nb, Ni, Fe, and Cr.

The variations observed in the chemical composition of the γ matrix in Table 2 and in the proxigrams in Fig. 4 and Fig. 5 occur due to the proximity of the matrix to the carbide and the Laves phase, respectively. While the composition of the matrix in Table 2 refers to a matrix only APM dataset (Fig. A2), the composition in the proxigrams show interphase boundary regions of few nanometers, where disturbances in the compositions are more pronounced.

3.3. Analysis of interphase region after direct ageing

Direct ageing causes the precipitation of γ′ and γ″ precipitates as seen

Table 1
Morphology of phases in as-build conditions.

	Grain size (μm)	GND density (10^{12}/m^2)	Solidification structure*	Laves vol. fraction (%)	Laves size (nm)	Dendritic arm spacing (nm)
Chess-AB	35 ± 26	153 ± 118	1	1.84	113 ± 66	-
			2	1.83	110 ± 63	977 ± 68
			3	1.97	150 ± 132	1006 ± 148
			4	2.04	154 ± 139	819 ± 116
Meander-AB	44 ± 31	175 ± 137	1	0.97	82 ± 49	-
			2	0.77	74 ± 94	352 ± 20
			3	1.00	66 ± 60	282 ± 28
			4	0.78	71 ± 52	425 ± 51
Chess-HA	86 ± 61	139 ± 104	-			
Meander-HA	83 ± 52	133 ± 115				

* according to sectioning orientation

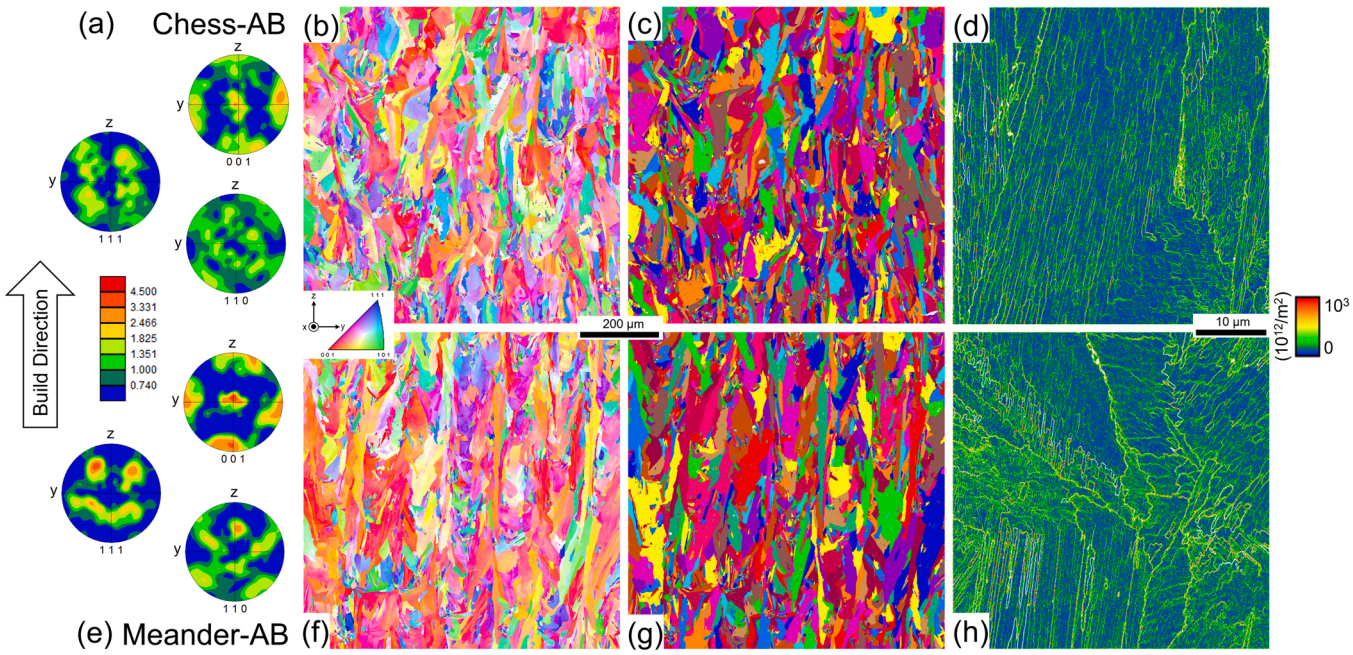

Fig. 2. EBSD images of typical as-built microstructures of Chess-AB (a) (001), (110) and (111) PFs, (b) IPF map, (c) grain map, (d) GND density map; EBSD images of as-built microstructure of Meander-AB (e) (001), (110) and (111) PFs, (f) IPF map, (g) grain map, (h) GND density map. The IPF color code was set with respect to the BD. (For interpretation of the references to colour in this figure legend, the reader is referred to the web version of this article.)

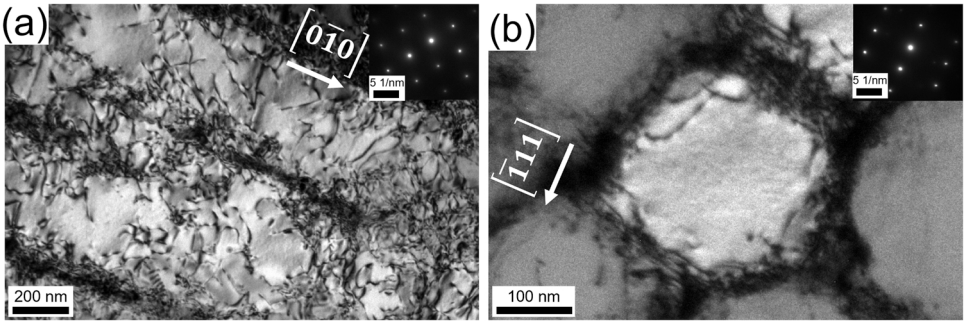

Fig. 3. Bright field TEM images of Meander-AB showing (a) dislocation rich region and (b) solidification formation with dislocation on the walls. Inset images show the selected area diffraction patterns where image (a) was obtained with **B**=[101] and **g**=[$0\bar{1}0$] and image (b) with **B**=[$1\bar{1}2$] and **g**=[$\bar{1}11$].

in Fig. 6 along with additional features. The detailed evolution of γ′ and γ″ precipitates will be examined in Section 3.5. Fig. 6a shows an APM reconstruction of an interface region containing nanoscale precipitates, a Cr and Mo rich phase, and a MC carbide. As shown in Fig. 6a, γ′ and γ″ precipitates are delineated by concentration isovalues of Al+Ti and Nb, respectively. The Cr and Mo rich phase might be a low Nb Laves phase based on its composition [16], being enclosed by a concentration isovalue of 7.07 at% of Mo, determined with the enhanced iso-surface concentration method [49]. This phase formed along a grain boundary separates a γ″ rich area to left hand side from a depleted region to the right. This is confirmed in Fig. 6b by the 1D compositional profile of the yellow cylinder that crosses the Laves phase. In the 5 nm range from 10 to 15 nm of the cylinder length, a large enrichment of Mo up to 12 at% and Cr to 36 at% is seen in addition to a sharp decrease in Ni concentration. The Fe composition is not greatly disturbed, while Nb, Ti and Al show a decreasing trend from left to right. Table 2 shows the chemical composition of the Laves phase and Fig. 6c shows the atom maps of the elements present. The C rich area is an indication of a MC carbide. B and P atoms along the Laves phase are another sign that this phase was formed along a grain boundary, since both elements are commonly segregated on this region [60].

3.4. Microstructure of chessboard and meander samples in the homogenized and aged conditions

The primary aim of the 1050 °C homogenization for 1 h was to achieve dissolution of the Laves phase. Fig. 7 shows BSE images of Chess and Meander conditions after HA. It can also be examined from Fig. 7 that Laves elimination has been achieved, however, some grain growth is observed. Fig. 7a and Fig. 7c show equiaxial grains alongside typical elongated grains also found in the AB condition. In the Chess-HA condition, these recrystallized grains are sparsely distributed throughout the microstructure as identified by the red arrows, while in Meander-HA they have formed preferentially along columns as shown in the center of the Fig. 7c, within the red dashed box. Annealing twins are observed in the recrystallized grains as identified by the red arrow. The higher magnification in Fig. 7b and Fig. 7d confirm Laves phase dissolution, and that no additional phases seem to pin the interface boundaries between sub-grain regions and equiaxed grains.

Similar to the AB materials, the pole figures (and the IPF map with respect to the BD) of the orientations of grains in HA samples are shown in Fig. 8a (Fig. 8b) and Fig. 8e (Fig. 8f) for Chess-HA and Meander-HA, respectively. The preferential orientation along the ⟨001⟩ direction is maintained, however, a double m.u.d intensity indicates that grain

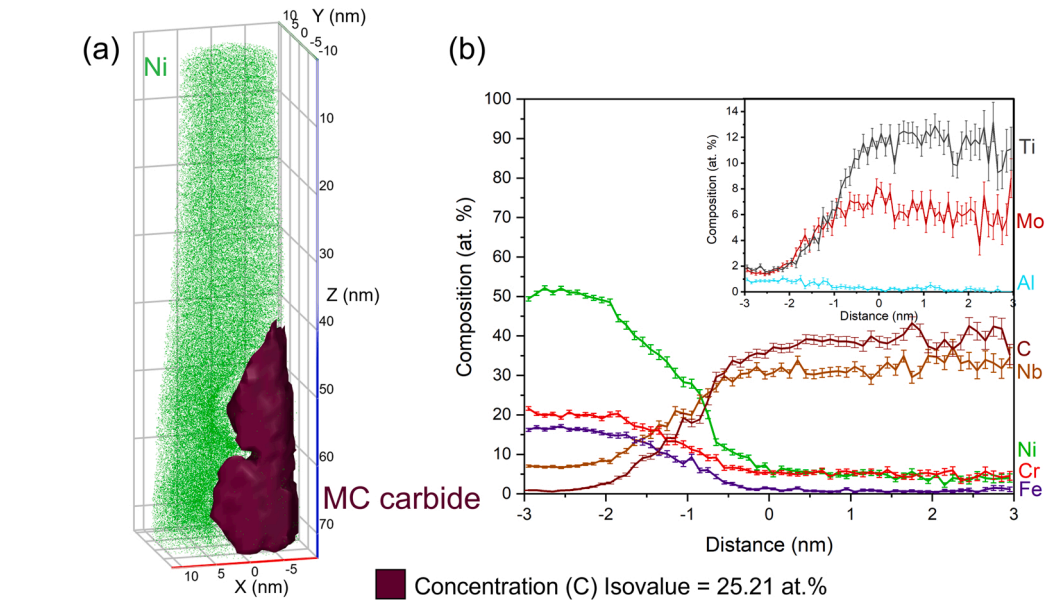

Fig. 4. APM reconstruction of interface region between γ matrix and MC carbide in (a) and proxigram in (b) in the Meander-AB condition. Enrichment of Ti, Mo, C, and Nb in the MC carbide are seen in the right half of the proxigram. (For interpretation of the references to colour in this figure legend, the reader is referred to the web version of this article.)

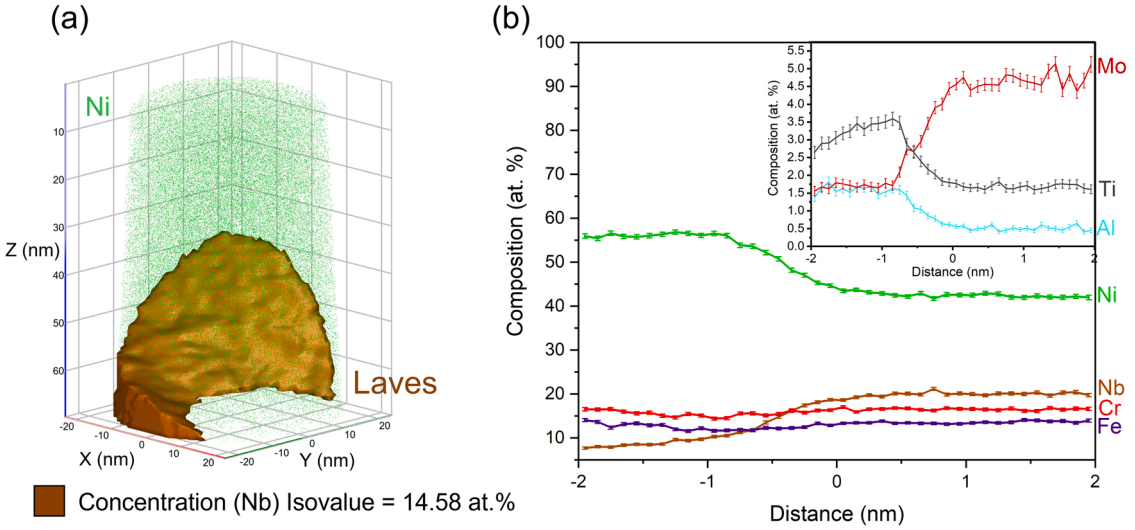

Fig. 5. APM reconstruction of interface region between γ matrix and Laves phase in (a) and proxigram in (b) in the Chess-AB condition. Enrichment of Mo, and Nb in the Laves phase are seen in the right half of the proxigram. (For interpretation of the references to colour in this figure legend, the reader is referred to the web version of this article.)

Table 2
Chemical composition of MC carbide, Laves phase, γ matrix, and low Nb Laves phase (at.%).

		Ni	Fe	Mo	Nb	Cr	Ti	Al	Si	C
MC carbide		4.98 ± 0.12	0.85 ± 0.05	6.30 ± 0.14	31.71 ± 0.34	5.18 ± 0.12	11.69 ± 0.19	0.19 ± 0.02	0.23 ± 0.03	38.68 ± 0.39
Laves phase		42.68 ± 0.11	13.46 ± 0.06	4.64 ± 0.03	19.77 ± 0.07	16.63 ± 0.06	1.72 ± 0.02	0.53 ± 0.01	0.25 ± 0.01	0.02 -
γ matrix	Chess-AB	52.00 ± 0.05	19.31 ± 0.03	1.37 ± 0.01	4.18 ± 0.01	21.10 ± 0.03	1.06 ± 0.01	0.74 ± 0.01	0.04 -	0.01 -
	Meander-AB	52.08 ± 0.05	19.31 ± 0.03	1.27 ± 0.01	4.60 ± 0.01	20.73 ± 0.03	1.01 ± 0.01	0.85 ± 0.01	0.03 -	- -
Low Nb Laves phase (Fig. 6)		26.75 ± 0.13	20.78 ± 0.11	12.10 ± 0.08	3.06 ± 0.04	36.35 ± 0.16	0.16 ± 0.01	0.11 ± 0.01	0.26 ± 0.01	0.03 -

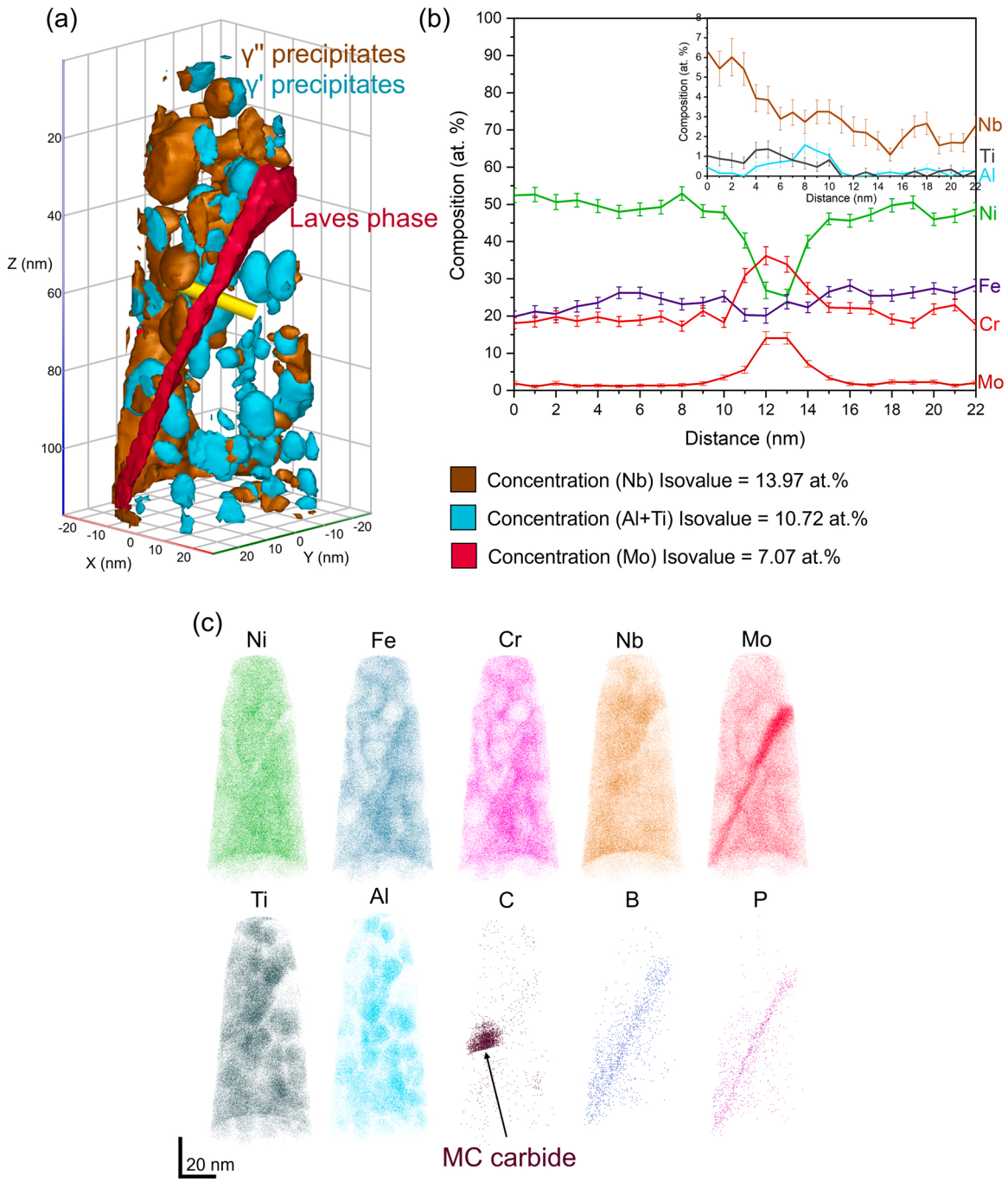

Fig. 6. (a) APM reconstruction of interface region containing γ′, γ′′ precipitates, Laves phase, and a MC carbide in Meander-DA. The compositional profile of the yellow cylinder in (a) is shown in (b); (c) Individual atom maps of the main elements in the tip. (For interpretation of the references to colour in this figure legend, the reader is referred to the web version of this article.)

growth occurred at a specific orientation still along the ⟨001⟩ direction [61–63]. The grain maps in Fig. 8c and Fig. 8g illustrate that grains are still elongated along the BD, however, as observed in Fig. 7, a column of fully recrystallized equiaxed grains is present in Meander-HA, as highlighted by the black dashed box in Fig. 8f. Supplementary Fig. A1c shows the distribution of grain sizes for both samples and respective fitted curves. Even though the distribution of grain size for Meander-HA and Chess-HA varies within a 40–200 μm range, their average grain size is roughly the same around 84 μm, as shown in Table 1. The HA heat treatment leads to grain growth in the order of 2.5 and 1.9 times in comparison to Chess-AB (35 μm) and Meander-AB (44 μm) samples, respectively. GND maps in Fig. 8d and Fig. 8h show that dislocation structures after HA seem to be more concentrated to the sub-grain boundaries and, to a lower degree, core of these sub-grains, in comparison to the AB conditions in Fig. 2. According to Table 1, the GND density is similar for both Chess-HA and Meander-HA (~ 136×10^{12} GND/m^2), however, the reduction from AB is more pronounced for the latter with a 24% decrease, while for the former it is only 9%. Similarly, to the AB condition, GND density analysis for HA materials should also consider the fitted curves shown in the GND density distribution in supplementary Fig. A1d. This underpins that varying GND densities are present between Chess-HA and Meander-HA.

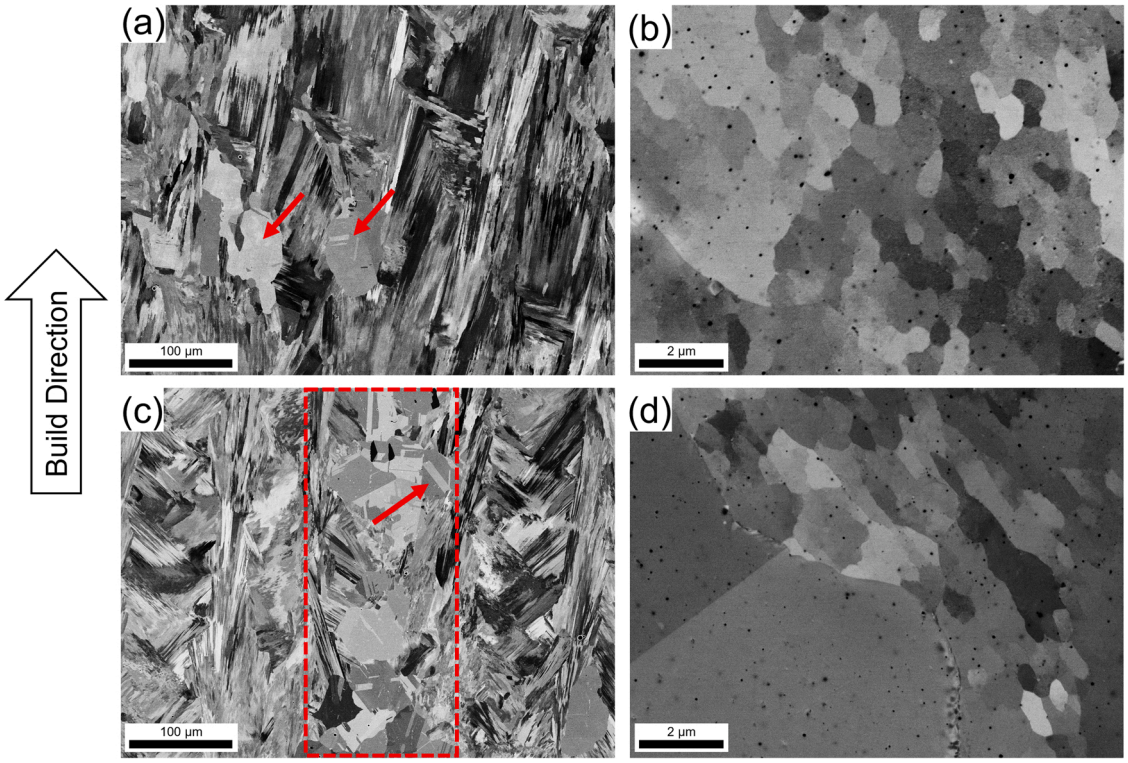

Fig. 7. (a) BSE image of Chess-HA with arrows indicating recrystallized grains; (b) higher magnification image of sub-grain region; (c) BSE image of Meander-HA with red dashed box indicating a column of recrystallized grains and arrow show a annealing twin, (d) higher magnification image of interface between a sub-grain region and a recrystallized grain. (For interpretation of the references to colour in this figure legend, the reader is referred to the web version of this article.)

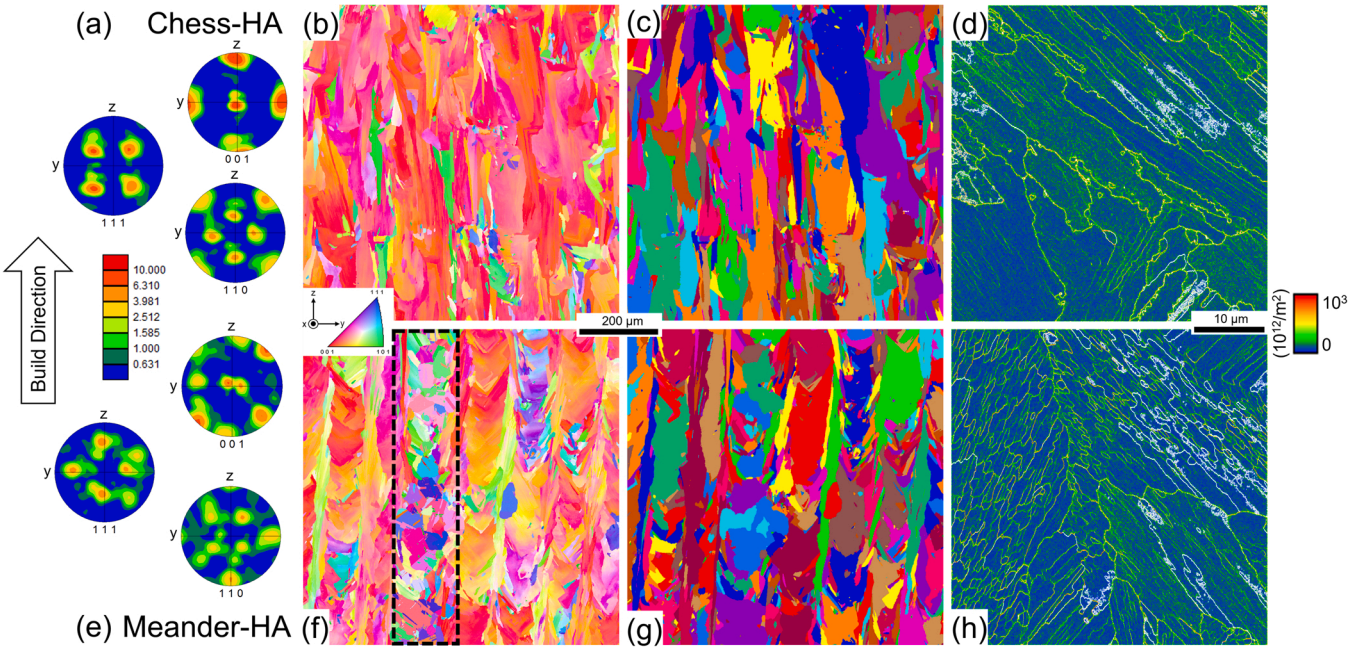

Fig. 8. EBSD images of typical microstructures of Chess-HA (a) (001), (110) and (111) PFs, (b) IPF map, (c) grain map, (d) GND density map; EBSD images of microstructure of Meander-HA (e) (001), (110) and (111) PFs, (f) IPF map with black dashed box showing a column of recrystallized grains, (g) grain map, and (h) GND density map. The IPF color code was set with respect to the BD. (For interpretation of the references to colour in this figure legend, the reader is referred to the web version of this article.)

3.5. Morphological analysis of γ′ and γ″ precipitates in direct aged versus homogenized and aged conditions

The availably of Al, Ti, and Nb in the γ matrix determines the formation of γ′ and γ″ precipitates. As shown in Table 2, Nb and Al solute concentrations available to form precipitates during ageing in Chess-AB (4.18 at% of Nb and 0.74 at% of Al) are lower than in Meander-AB (4.6 at% of Nb and 0.85 at% of Al). Fig. 9 shows the APM

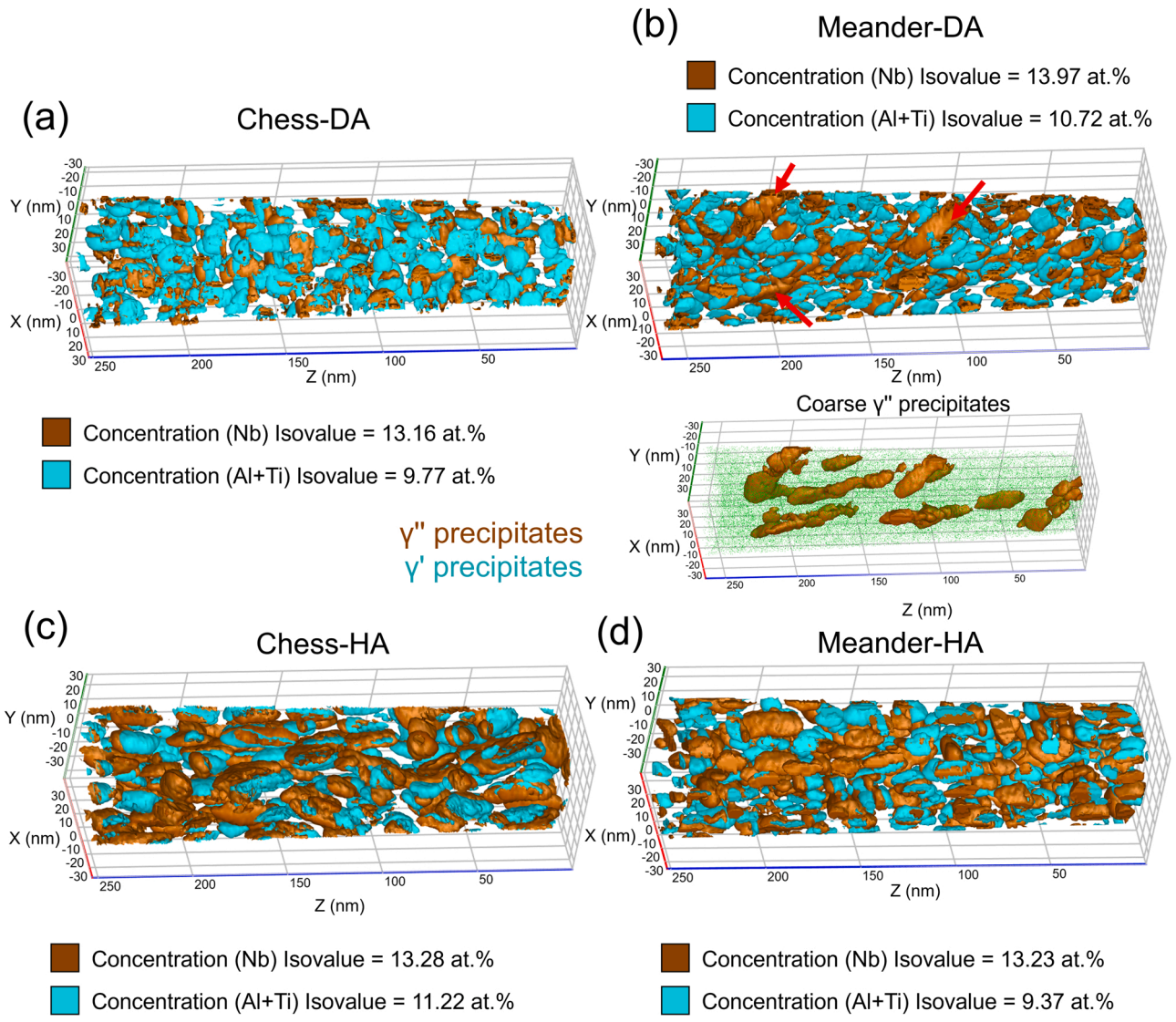

Fig. 9. APM reconstruction showing γ′ and γ′′ precipitates in (a) Chess-DA; (b) Meander-DA and coarse γ′′ precipitates marked by red arrows and shown separated from other precipitates and Ni ions in green; (c) Chess-HA; and (d) Meander-HA. (For interpretation of the references to colour in this figure legend, the reader is referred to the web version of this article.)

reconstruction of DA and HA samples away from interdendritic phases, with γ′ colored in turquoise and γ′′ in brown. Concentration isovalues of Nb and Al+Ti for each condition are displayed alongside the APM images. These values change for each condition because the composition of the precipitates also change. A single isovalue of Nb and Al+Ti would not properly take this variation into consideration. Marked by red arrows, coarse and elongated γ′′ precipitates are visible in Meander-DA in Fig. 9b, which are shown isolated from other precipitates in the bottom reconstruction. These coarse γ′′ precipitates are not present in Chess-DA in Fig. 9a. Precipitates are also identified in Chess-HA in Fig. 9c and Meander-HA in Fig. 9d, however, no coarse phases are present in these samples.

Fig. 10 shows quantitative analyses of the precipitates from Fig. 9. Volume fraction plots in Fig. 10a show that except for a minor variation in Meander-DA, the scanning strategy and heat treatment do not heavily affect γ′ precipitation. For γ′′, a significant variation in volume fraction is observed, where Chess-HA has quadruple volumes (16.4%) of this phase in comparison to Chess-DA (4%). If the 3.7% volume fraction of coarse γ′′ precipitates in Meander-DA is disregarded, the volume fraction of nanoscale precipitates is similar to Chess-DA, and a threefold increase is seen for Meander-HA (13%). The length of the major axis of the precipitates is shown in Fig. 10b. Both γ′ and γ′′ in Chess-DA and Meander-DA have sizes around 14 nm, while for HA condition, the former increases to 19 nm for Meander-HA and the latter increase to 25 and 21 nm for Chess-HA and Meander-HA, respectively. Coarse γ′′ major axis length range from 25 to 55 nm.

The bubble plots in Fig. 11 illustrate the aspect ratio versus oblateness of γ′ and γ′′ precipitates according to their volume. In case of Meander-DA, the average shape of commonly spherical γ′ precipitates falls into the sphere quadrant at oblateness of 0.63, while in Chess-DA these precipitates trend towards a disc morphology to an average oblateness of 0.48 in the disc quadrant. In these conditions, γ′′ shows similar behavior being more disc shaped in the Chess-DA (oblateness of 0.5) than in Meander-DA (oblateness of 0.66). In the HA samples, for the chessboard strategy, the shape of the γ′′ is unchanged in comparison to DA. For Meander-HA lower oblateness values are observed for γ′′, with an average value of 0.56. The γ′ precipitates in HA are slightly more spherical than in DA samples for the chessboard strategy, with oblateness of 0.53, while for Meander-HA lower spherical shape is identified at oblateness of 0.61. The coarse γ′′ precipitates, found in the Meander-DA sample, are represented by the larger dark bubbles in Fig. 11b, having an average shape in the rod quadrant.

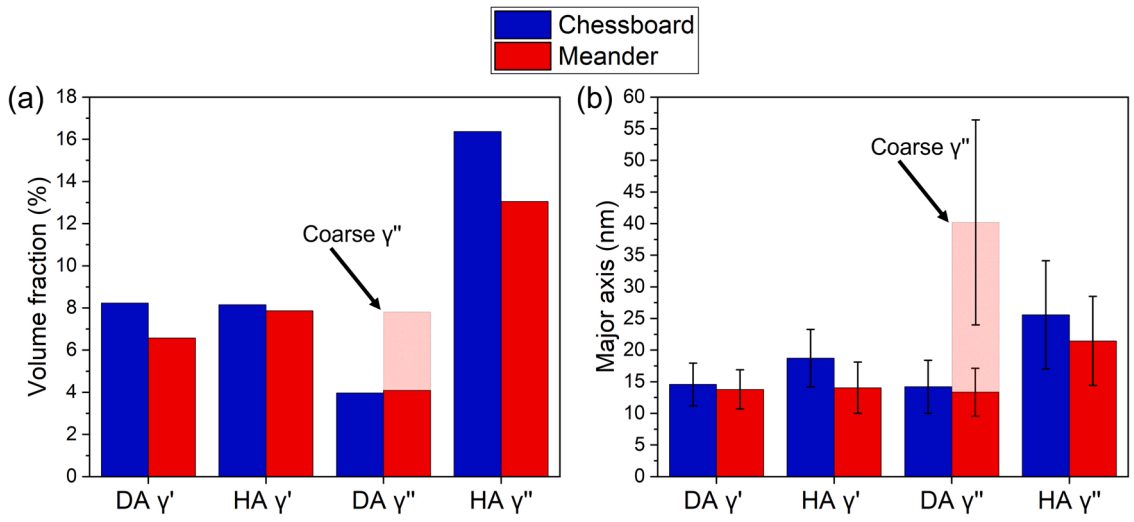

Fig. 10. (a) Volume fraction and (b) average length of major axis of γ' and γ'' precipitates. (For interpretation of the references to colour in this figure legend, the reader is referred to the web version of this article.)

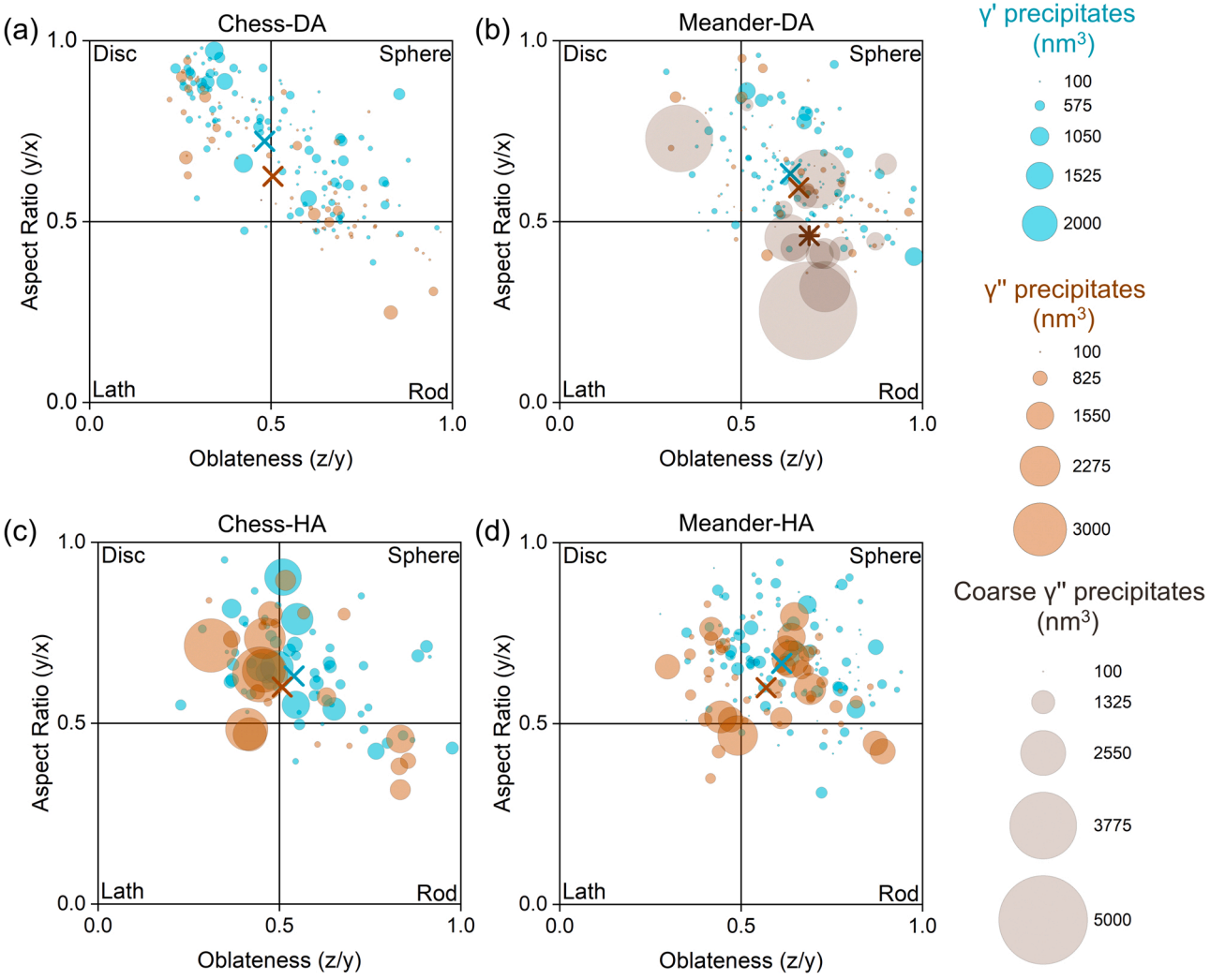

Fig. 11. Aspect ratio vs oblateness of γ' and γ'' precipitates in (a) Chess-DA; (b) Meander-DA; (c) Chess-HA; (d) Meander-HA. Crosses represent the average value of aspect ratio vs oblateness. The star in (b) is the average aspect ratio vs oblateness of the large darker circles that represent the coarse γ'' precipitates. The radii of the bubbles are directly proportional to their volume. (For interpretation of the references to colour in this figure legend, the reader is referred to the web version of this article.)

Good correlation of the precipitate's morphology is observed with APM results from literature for IN718 manufactured under different conditions [59,64,65]. However, it is important to highlight possible local magnification artifacts that may occur in APM experiments due to differences in evaporation fields of the many phases present [66]. For this reason, correlative characterization analyses with TEM and small-angle X-ray scattering are recommended for future works to complement our findings.

3.6. Chemical composition evolution of γ′ and γ″ precipitates

Fig. 12 shows the evolution of chemical composition of the precipitates in DA and HA samples. For the γ′ precipitates in Fig. 12a, small variations are observed confirming that printing and post-processing parameters have low impact on the evolution of these precipitates, as previously discussed. The largest variation is for Mo in Chess-DA (1.32 at%) which is more than double than in Meander-DA (0.58 at%) and higher than the HA condition (0.61 at% for Chess-HA and 0.89 at% for Meander-HA). The composition of γ″ precipitates in Fig. 12b is shown for DA and HA for typical precipitates, while the composition of

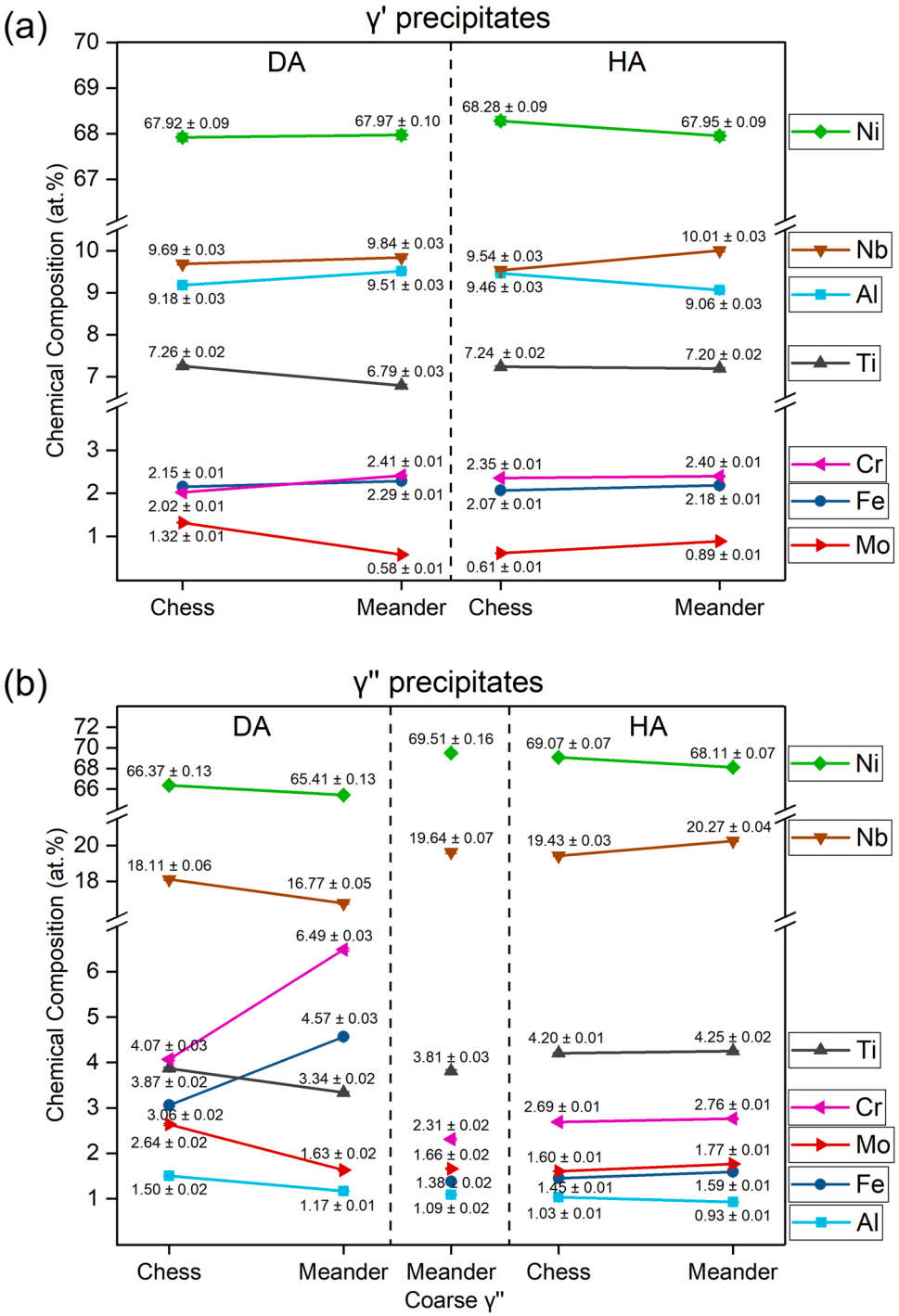

Fig. 12. (a) Chemical composition of γ′ precipitates; (b) Chemical composition of γ″ precipitates. (For interpretation of the references to colour in this figure legend, the reader is referred to the web version of this article.)

the coarse γ″ precipitates in Meander-DA is shown in the middle of the chart. Larger compositional variations are observed for all elements in comparison to γ′. In DA, concentration of Ni, Nb, and Ti in the γ″ precipitates is significantly lower than in HA, while Cr, Fe, Mo, and Al concentrations are higher. The average variation in composition between Chess-DA and Meander-DA is five times higher than variations between Chess-HA and Meander-HA, indicating that precipitates formed after HA are more compositionally stable. Coarse precipitates in Meander-DA have a compositional profile closer to the precipitates in HA condition. It should be mentioned that error bars are included in the graphs in Fig. 12, however, these deviations are negligible and cannot be easily seen with the chosen axis dimensions.

3.7. Hardness testing

The micro- and nanostructural features presented in Fig. 1 to Fig. 12 affect the mechanical properties. Fig. 13 shows the evolution of hardness according to the condition of the material, i.e., AB, DA, and HA for meander and chessboard scanning strategies. DA causes a 57% increase in hardness in relation to AB condition from 340 HV to 535 HV, while HA materials have around 40% higher hardness. No significant difference is observed between the two scanning strategies for AB and DA, while a 15 HV difference is observed between Chess-HA and Meander-DA, however, these hardness values are within each other's standard deviation. Superior mechanical strength is expected for the heat treated materials [58] as hardness has been demonstrated to correlated with ultimate tensile strength (UTS) [67], while some of the current authors have shown in their previous studies on cast and wrought IN718 that the hardness was a good representation of the yield strength (YS) at 650 °C [68]. For more details on the mechanical properties of the AB materials, the reader is referred to [46].

4. Discussion

4.1. Effects of scanning strategy on the as-built microstructure

The length of the scanning vectors plays an important role in the temperature distribution during the LPBF process [69]. In the meander scanning strategy, the length of the scanning vector is equal to the x or y dimension of the fabricated block (Fig. 1e), i.e., 140 or 22 mm, respectively. In the chessboard strategy, this vector is always equal to 5 mm, which is the size of the islands (Fig. 1a). In IN718, due to the large conductivity difference between powder (0.1190 W/m/°C) and solid

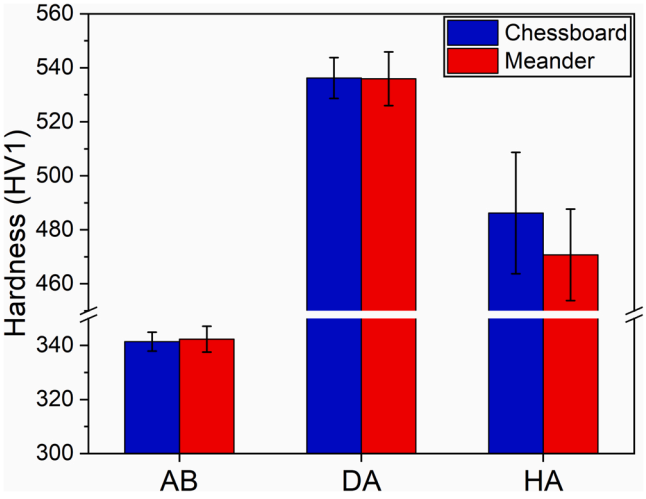

Fig. 13. Vickers hardness (HV1) of chessboard and meander samples in AB, DA, and HA condition. (For interpretation of the references to colour in this figure legend, the reader is referred to the web version of this article.)

(31.3 W/m/°C) at 1350 °C [70], heat dissipation during cooling after the laser track passing is directly related to the length of the scanning vector [19]. A shorter vector length, and thus shorter time interval between solidification and reheating along a single laser track due to melting of the neighboring laser track, leads to higher temperature fields in the deposited layers and slower cooling rates [69]. The cooling rate (ε) at the solidification front determines the size of the dendritic arm spacing (λ) according to $\lambda = a\varepsilon^{-b}$ [71], with a and b being material constants. Liu et al. [72] found that in steels dendritic substructure size varies according to solidification rates for different processing parameters. As a result, coarser dendritic structures and lower residual stresses are expected in Chess-AB as shown in Fig. 1 and Fig. 2 in agreement with previous research [20,73]. Table 1 reports that solidification structures are 2–3.6 times larger in Chess-AB. The GND density, which is correlated to the residual stress from reheating and cooling cycles, is 14% lower in Chess-AB. The dislocation network in the Meander-AB condition (Fig. 3) is mainly located in the interdendritic regions due to the presence of secondary phases, but also arranged into low angle boundaries in order to accommodate misorientations between dendrites. The presence of GNDs in the dendritic cores is another indication for the high level of stresses generated during the cyclic and rapid remelting and solidification [22,74].

The correlation between G and V controls the morphology evolution of the dendrites [75] where an increase in constitutional undercooling promotes the solidification front to change from planar to dendritic. In the interdendritic regions, liquid with high concentration of Nb, Mo, and Ti solidifies into eutectic phase composed of γ and TCP phases, such as the Laves phase [18]. In the Meander-AB sample, as shown in Table 1, low volume fractions (0.88%) of discrete Laves phase particles are found due to less pronounced chemical segregation associated with the high cooling rate around the liquid-solid front. In the Chess-AB condition, double volume fractions (1.92%) of chain-like Laves phase particles are identified in agreement with the lower solidification rate due to higher temperatures in the liquid-solid interface induced by previous laser tracks.

The melt pool shapes seen in the LOM in Fig. 1 and the directional grain growth in EBSD maps in Fig. 2 can be correlated to the scanning strategies and are governed by the Marangoni effect and associated convective phenomena [76]. Even though both strategies have a repetition of the pattern at every other layer due to the 90° rotation, the arc shaped melt pools generated by the Gaussian energy distribution of the laser beam [13] are consistently more homogeneous in Meander-AB. The scanning vector length within the chessboard islands causes higher temperature fields within each single layer. However, in the layer $n + 1$, the islands are randomly scanned and laterally shifted by 1 mm compared to islands in layer n, meaning that a much lower regular repetition is present in this scanning strategy when compared to the meander strategy. During solidification, the overlapping melt pools in the chessboard pattern generates a distribution of grains, which tend to be confined within the 30 μm thick layers. Conversely, the more homogeneous meander pattern promotes a heat flux between layers where epitaxial grain growth is favored, crossing the MPBs and producing larger elongated grains with stronger cubic texture along the BD as shown in Fig. 2 [22].

4.2. TCP phases and MC carbides at interphase boundaries

The eutectic transformation during solidification occurs when the Nb concentration in the liquid is within 15–20 at% range, causing Laves phase formation [77]. Prior to that, MC carbides enriched in Nb and Ti are formed [78]. Spherical MC carbides can become nucleation sites as they have been found embedded in the Laves phase in the Meander-AB condition [46]. As shown by the APM reconstructions in Fig. 4 and Fig. 5 and chemical information in Table 2, these precipitates are responsible for consuming Nb from the γ matrix, impacting the formation of the

main strengthening precipitates during ageing. The formation of the low Nb Laves phase has a significant detrimental impact on mechanical properties, due to grain boundary embrittlement. As shown in Fig. 6, this phase also promotes uneven distribution of Nb, and consequently the formation of a γ″ depleted zone is seen in the grain on the right-hand side of the tip.

4.3. Heat treatment effects on the microstructure

Post-processing treatments are applied to minimize some of the microstructural in homogeneities from the AM process, and to precipitate nanoscale strengthening phases. While direct ageing (i.e. ageing without a solution treatment) in cast and wrought IN718 is economical and reported to achieve excellent combinations of mechanical properties [65,79,80], typical ageing temperatures alone are not sufficient to produce significant microstructural changes related to grain size, Laves phase, and residual stresses after AM [37,43]. Homogenization at temperatures above 1000 °C, on the other hand, may cause phase dissolution, as well as recrystallization and grain growth. The Laves solvus temperature is reported to be around 1100 °C [81], however, lower homogenization temperatures have shown to be able to dissolve this phase when it is present in low volumes. The homogenization curve proposed by Huang et al. [30] places the homogenization temperature and duration selected in our investigation at the threshold of where significant microstructural changes are expected to occur. This was done intentionally as will be discussed later. As seen in Fig. 7, Laves phase dissolution is achieved for Chess-HA and Meander-HA, however, additional and localized recrystallization takes place in the latter. The lower volume fraction of Laves phase in Meander-AB (Table 1) enables faster dissolution of this phase, which has been shown to be an effective sub-grain boundary pinning particle [34]. Recrystallization then proceeds primarily during homogenization of this condition. Due to its epitaxially grown grains structures (Fig. 2), this initial recrystallization is confined to columns of closely oriented grains, producing a multi-modal grain distribution [82]. In the Chess-HA condition in Fig. 7, recrystallization seems to occur more randomly, possibly within prior AB grains where the Laves phase volume fraction was lower. Overlapping melt pool areas which contain higher residual stresses might also lead to accelerated recrystallization due to existence of higher number of heterogenous nucleation sites [83,84].

For overall mechanical properties improvements, a complete Laves phases elimination is recommended, while the grain size should remain small. Sub-grain boundaries such as those from the dendritic structures are also beneficial to strength, as they limit dislocation slip, while low fractions δ phase on the grain boundaries are reported to limit grain growth enhancing fatigue properties in conventionally manufactured materials [33,85]. These complex interplays highlight the importance of optimization of heat treatment schedules. On the one hand, low homogenization temperatures might lead to δ phase precipitation and smaller grain sizes, however, Laves phase dissolution might not be achieved. High homogenization temperatures, on the other hand, will remove the Laves phase, but formation of the δ phase will not occur causing grain growth. For industrial applications, shorter homogenization at lower temperatures is more economically viable, however, higher temperatures and longer heat treatments might better remove heterogeneities in the material. Zhao et al. [86] showed recently that at 1180 °C, grain growth occurs primarily in the first 20 min of homogenization, while longer treatments up to 12 h do not seem to cause any significant additional grain growth. We have chosen an intermediate homogenization temperature of 1050 °C for a short time of 1 h, to eliminate the Laves phase, while retaining most of the original dendritic structure and avoiding δ phase formation which consumes Nb from the γ matrix [87]. According to Table 1, grains have more than doubled in size in Chess-HA, while the GND density decreased only by 9%. The grain size increase in the Meander-HA sample (Fig. 8) was slightly lower than the chessboard sample, while the GND density reduction of 24% was more substantial. As discussed in the next section, the influence of the main strengthening precipitate γ″ volume and size is significantly different between DA and HA materials, however, the grain size, and the presence of retained dislocation networks need to be taken into account when considering the average 10% difference in hardness between these conditions (Fig. 13). Both factors act as barriers for the slip of dislocations created during hardness testing. Generally, there is a direct correlation between hardness, room temperature UTS and YS [67,68], however, these properties have not been shown to significantly vary between DA and HA materials [11,17,88]. For instance, YS in the order of 1200 MPa have been found for DA and HA materials, while UTS in the 1400–1500 MPa have been reported. Other critical mechanical properties, however, such as ductility and fatigue resistance are expected to be superior in the HA samples, due to the removal of the brittle Laves phase [17]. Deng et al. [11] found that during tensile testing of vertically built IN718, in comparison to DA, elongation to fracture is 10% higher in samples subjected to a heat treatment similar to HA.

4.4. Nanoscale precipitation behavior as a function of heat treatment and scanning strategy

The in-situ formation of precipitates has been reported during controlled LPBF processing [89]. Using the processing parameters in the current study, no precipitation is identified as confirmed by the absence of superlattice reflections in the SAED in Fig. 3. However, atomic clustering was found as shown in Fig. A2b for Chess-AB. The experimental curve of Al atoms which are prone to clustering [59], exhibits a slight deviation from the randomized curve. This is an indication that due to the high temperatures fields at the short laser scanning vector, the cooling rate in this sample is low enough to allow Al diffusion towards positions that could become nucleation sites for γ′ precipitates. For both scanning strategies, after DA and HA, γ′ precipitation is largely independent of previous processing. In agreement with the unaltered morphology evolution, the chemical evolution of γ′ also does not show significant variations during DA versus HA as reported in Fig. 12a, as only negligible amounts of Al and Ti are incorporated into the Laves phase, i.e., its dissolution does not release much additional Al and Ti into the matrix.

The microsegregation of elements to interdendritic regions is a common issue in AM IN718 [17,41]. The dendritic core is poor in Nb, which can be related to the low volume fractions (~ 4%) of nanoscale γ″ as found in both Chess-DA and Meander-DA samples (Fig. 9 and Fig. 10). The presence of Nb rich areas at the interdendritic regions surrounding Laves phase particles will cause the formation of coarse γ″ precipitates. In this case, the size of precipitates has been shown to be in the undesirable size range of hundreds of nanometers [35]. The Meander-DA condition with a higher GND density has a higher probability of locating coarse γ″ precipitates that are formed along dislocation structures within an atom probe dataset, similarly to the phenomenon observed in highly strained conventionally manufactured IN718 [59,90]. Even though the APM samples studied were from random regions, the length of the major axis of coarse precipitates of ~40 nm (Fig. 10b) allows the conclusion that the tips in Fig. 9b show a dislocation rich dendritic core region, instead of an interdendritic area. Fig. 3a shows that these regions contain entangled dislocations (Fig. 3a) in the AB condition, and consequently in the DA condition too. Therefore, the formation of the coarse precipitates was accelerated by pipe diffusion due to the dislocation network [91]. The lower volume fraction of the Laves phase in Meander-AB (Table 1) also contributes to the formation of the coarse γ″ precipitates since the γ matrix has higher Nb contents (Table 2). Similar structures may be present in the Chess-DA condition, however, they are less likely to be contained in APM samples due to the lower GND density and lower Nb concentration in the matrix.

The influence of Laves phase dissolution during homogenization is more pronounced for γ″ precipitates. In addition to the redistribution of Nb into the matrix and minimizing Nb segregation, dislocation

annihilation also decreases the likelihood of formation of coarse γ″ in the HA conditions. As shown in Fig. 10a, the increase in volume fraction to 16% and 13% and average length to 25 and 21 nm for Chess-HA and Meander-HA, respectively, indicate that this heat treatment produces γ″ precipitate morphologies closer to conventionally manufactured and aged IN718 materials [90]. According to Fig. 12b, the precipitates in HA conditions have compositions that are more stable and comparable to other processing routes [59] than the DA condition. In DA conditions, γ″ precipitates are enriched in Fe, Cr, and Mo and slightly depleted in Nb. The lower amount of Nb in γ″ in the DA condition can be justified by the presence of the Laves phase. First-principles calculations have shown the influence of alloying elements of the phase stability of γ″ [92–94], where Cr and Fe tend to occupy the Ni sublattice, while Mo substitute the Nb sublattice. However, further density functional theory studies might clarify this aspect of non-ideal stoichiometry for the γ″ precipitates after DA in LPBF IN718. The coarse γ″ precipitates in Meander-DA have compositions closer to the precipitates found in Chess-HA and Meander-HA. As in the DA condition, the accelerated diffusion of heavy elements along dislocations enables their redistribution along these channels, thus more compositionally stable coarse precipitates are formed [59]. In the HA condition, the elements are already more homogenously distributed after homogenization, and precipitates formed have more typical morphologies and chemical compositions.

Concerning the morphology of the precipitates as presented in Fig. 11, their average aspect ratio to oblateness is consistent to previous reports on conventionally manufactured IN718 parts [59,90]. The γ″ precipitates after HA seem to correspond more closely to the literature with respect to the lower oblateness levels towards a disc shape of 0.5 and 0.56 for Chess-HA and Meander-HA, respectively. Thermo-kinetic models of conventionally manufactured IN718 show the length of the major axis of γ″ to range from 15 to 20 nm, at volume fractions of 11% and oblateness of 0.32. The γ′ precipitates are reported to be smaller with a mean length between 12 and 16 nm, volume fractions from 7% to 9%, and oblateness of 0.54 [79,95].

The strengthening effect related to the precipitate-dislocation interaction can occur by the shearing mechanism where dislocations cut small precipitates or the Orowan mechanism where dislocations bow-out between large precipitates [96]. The strengthening contribution depends on the fraction and size of precipitates. For volumes fractions between 9% and 15% of γ″, optimal contribution have been reported by Zhang et al. [88] for precipitates diameter between 34 and 44 nm. Accordingly, the larger precipitates in the HA samples are expected to generate higher strengthening than the smaller precipitates in the DA samples. However, the presence of Laves phase and dislocations cells in the latter also provide additional hardening. Laves phase has been shown to contribute to as much as 107.9 MPa in yield strength [88]. When converted to HV, according to the relation proposed by Osada et al. [97], up to 44 HV can be attribute to the Laves phase. The values of ~536 HV for DA, and 470–486 HV for HA materials are also impacted by the grain structure and retained dislocation networks, as discussed in Section 4.1, where the smaller grains and higher fraction of dislocation cells in DA condition contribute to increased hardness.

5. Conclusions

In this study, new insights into the detailed microstructure evolution in IN718 materials processed by laser powder-bed fusion are presented, with particular emphasis on the morphology and chemistry of secondary phases. The influence of scanning strategy is considered for Meander and Chessboard strategies. Further, the microstructural effects of direct ageing (DA) versus homogenization and ageing (HA) heat treatments are studied in detail. The key finding can be summarized as follow:

- The shorter scanning vector length in the Chessboard strategy results in slower heat dissipation, generating coarser interdendritic arm spacing with the formation of double volume fractions of ~80% larger Laves phase than in Meander-AB. Slower cooling also leads to Al clustering in Chess-AB. The higher regularity in the Meander strategy generates coarse grains epitaxially grown along the build direction.
- Atom probe microscopy reveals MC carbides rich in Nb, Ti, and Mo, and Laves phase with high concentrations of Nb, Mo, Fe, and Cr. A Cr-Fe-Mo rich acicular phase on a grain boundary is identified as low Nb Laves phase.
- HA eliminates the Laves phase but causes grain growth and partial recrystallization. In Meander-HA, recrystallized grains are formed along columns, possibly where large epitaxial grains where located. Dislocation annihilation is more pronounced in the Meander samples.
- Low availability of solute elements in the matrix due to the presence of Laves phase and MC carbides impacts γ″ precipitation. The volume fraction of nanoscale γ″ is around 4% in both Chess-DA and Meander-DA conditions. The Meander-DA condition contains coarse precipitates formed by pipe diffusion. The dissolution of the Laves phase after HA leads to more desirable volume fractions of nanoscale γ″ of ~16%.
- Coarse γ″ precipitates in Meander-DA have chemical compositions close to chemically stable precipitates in the HA condition. Due to the inhomogeneous distribution of alloying elements on the matrix after LPBF, γ″ precipitates in the DA condition are enriched in Mo, Cr, and Fe, and low in Nb. The morphology and chemical composition of γ′ precipitates are not significantly impacted by the scanning strategy or heat treatment.
- The higher hardness after heat treatment is mostly caused by γ′ and γ″ precipitation, however, the larger grain size, lower GND density, and dissolution of Laves phase in the HA condition contribute to lower hardness than the DA samples.

We believe that these new detailed findings will enable optimizations of processing and post-processing parameters. They will also provide useful input data for CALPHAD and thermo-kinetic modelling for achieving superior mechanical properties in LPBF IN718.

CRediT authorship contribution statement

Vitor Vieira Rielli: Conceptualization, Methodology, Formal analysis, Investigation, Validation, Writing – original draft, Project administration, Writing – review & editing. **Alessandro Piglione:** Investigation, Formal analysis, Writing – review & editing. **Minh-Son Pham:** Supervision, Resources, Writing – review & editing. **Sophie Primig:** Supervision, Resources, Writing – review & editing, Funding acquisition.

Declaration of Competing Interest

The authors declare that they have no known competing financial interests or personal relationships that could have appeared to influence the work reported in this paper.

Acknowledgements

This research is funded by the Australian Research Council Linkage Project LP190101169. S. Primig is further supported by the Australian Research Council DECRA (DE180100440) and UNSW Scientia Fellowship schemes. The authors thank Dr. Simon Hager for technical assistance and use of facilities supported by Microscopy Australia at Electron Microscope Unit at the Mark Wainwright Analytical Centre at UNSW, and Dr. Takanori Sato and Prof. Simon P. Ringer at the Australian Centre for Microscopy and Microanalysis at the University of Sydney. The authors thank Dr. Bonnie Attard and Dr. Moataz M. Attallah at the University of Birmingham for the fabrication of the specimens. A. Piglione and M.-S. Pham would like to thank the Beijing Institute of Aeronautical

Materials (BIAM) and the BIAM - Imperial Centre for Materials Characterisation, Processing and Modelling at Imperial College London for their support.

Appendix A. Supporting information

Supplementary data associated with this article can be found in the online version at doi:10.1016/j.addma.2021.102540.

References

[1] S. Singamneni, Y. LV, A. Hewitt, R. Chalk, W. Thomas, D. Jordison, Additive manufacturing for the aircraft industry: a review, J. Aeronaut. Aerosp. Eng. 08 (2019), https://doi.org/10.35248/2168-9792.19.8.215.

[2] S. Mohd Yusuf, S. Cutler, N. Gao, Review: the impact of metal additive manufacturing on the aerospace industry, Met 9 (2019), https://doi.org/10.3390/met9121286.

[3] R. Liu, Z. Wang, T. Sparks, F. Liou, J. Newkirk, Aerospace applications of laser additive manufacturing, in: Laser Addit. Manuf., Elsevier, 2017, pp. 351–371.

[4] F.H. Froes, R. Boyer, Additive manufacturing for the aerospace industry, Elsevier,, 2019.

[5] M. Pröbstle, S. Neumeier, J. Hopfenmüller, L.P. Freund, T. Niendorf, D. Schwarze, M. Göken, Superior creep strength of a nickel-based superalloy produced by selective laser melting, Mater. Sci. Eng. A 674 (2016) 299–307, https://doi.org/10.1016/j.msea.2016.07.061.

[6] C.K. Yong, G.J. Gibbons, C.C. Wong, G. West, A critical review of the material characteristics of additive manufactured in718 for high-temperature application, in: Metals, 10, Basel, 2020, pp. 1–22, https://doi.org/10.3390/met10121576.

[7] E.M. Fayed, M. Saadati, D. Shahriari, V. Brailovski, M. Jahazi, M. Medraj, Optimization of the post-process heat treatment of inconel 718 superalloy fabricated by laser powder bed fusion process, in: Metals, 11, Basel, 2021, pp. 1–27, https://doi.org/10.3390/met11010144.

[8] B. Diepold, N. Vorlaufer, S. Neumeier, T. Gartner, M. Göken, Optimization of the heat treatment of additively manufactured Ni-base superalloy IN718, Int. J. Miner. Metall. Mater. 27 (2020) 640–648, https://doi.org/10.1007/s12613-020-1991-6.

[9] M.E. Aydinöz, F. Brenne, M. Schaper, C. Schaak, W. Tillmann, J. Nellesen, T. Niendorf, On the microstructural and mechanical properties of post-treated additively manufactured Inconel 718 superalloy under quasi-static and cyclic loading, Mater. Sci. Eng. A. 669 (2016) 246–258, https://doi.org/10.1016/j.msea.2016.05.089.

[10] J. Schröder, T. Mishurova, T. Fritsch, I. Serrano-Munoz, A. Evans, M. Sprengel, M. Klaus, C. Genzel, J. Schneider, G. Bruno, On the influence of heat treatment on microstructure and mechanical behavior of laser powder bed fused Inconel 718, Mater. Sci. Eng. A. 805 (2021), https://doi.org/10.1016/j.msea.2020.140555.

[11] D. Deng, R.L. Peng, H. Brodin, J. Moverare, Microstructure and mechanical properties of Inconel 718 produced by selective laser melting: sample orientation dependence and effects of post heat treatments, Mater. Sci. Eng. A. 713 (2018) 294–306, https://doi.org/10.1016/j.msea.2017.12.043.

[12] S. Hocine, H. Van Swygenhoven, S. Van Petegem, C.S.T. Chang, T. Maimaitiyili, G. Tinti, D. Ferreira Sanchez, D. Grolimund, N. Casati, Operando X-ray diffraction during laser 3D printing, Mater. Today 34 (2020) 30–40, https://doi.org/10.1016/j.mattod.2019.10.001.

[13] S. Hocine, H. Van Swygenhoven, S. Van Petegem, Verification of selective laser melting heat source models with operando X-ray diffraction data, Addit. Manuf. 37 (2021), 101747, https://doi.org/10.1016/j.addma.2020.101747.

[14] L. Nastac, J.J. Valencia, M.L. Tims, F.R. Dax, Advances in the solidification of IN718 and RS5 Alloys, Superalloys 718 (2001) 625–706.

[15] N. Raghavan, R. Dehoff, S. Pannala, S. Simunovic, M. Kirka, J. Turner, N. Carlson, S.S. Babu, Numerical modeling of heat-transfer and the influence of process parameters on tailoring the grain morphology of IN718 in electron beam additive manufacturing, Acta Mater. 112 (2016) 303–314, https://doi.org/10.1016/j.actamat.2016.03.063.

[16] R. Krakow, D.N. Johnstone, A.S. Eggeman, D. Hünert, M.C. Hardy, C.M.F. Rae, P. A. Midgley, On the crystallography and composition of topologically close-packed phases in ATI 718Plus®, Acta Mater. 130 (2017) 271–280, https://doi.org/10.1016/j.actamat.2017.03.038.

[17] S. Sui, H. Tan, J. Chen, C. Zhong, Z. Li, W. Fan, A. Gasser, W. Huang, The influence of Laves phases on the room temperature tensile properties of Inconel 718 fabricated by powder feeding laser additive manufacturing, Acta Mater. 164 (2019) 413–427, https://doi.org/10.1016/j.actamat.2018.10.032.

[18] P. Nie, O.A. Ojo, Z. Li, Numerical modeling of microstructure evolution during laser additive manufacturing of a nickel-based superalloy, Acta Mater. 77 (2014) 85–95, https://doi.org/10.1016/j.actamat.2014.05.039.

[19] H. Jia, H. Sun, H. Wang, Y. Wu, H. Wang, Scanning strategy in selective laser melting (SLM): a review, Int. J. Adv. Manuf. Technol. 113 (2021) 2413–2435, https://doi.org/10.1007/s00170-021-06810-3.

[20] B. Cheng, S. Shrestha, K. Chou, Stress and deformation evaluations of scanning strategy effect in selective laser melting, Addit. Manuf. 12 (2016) 240–251, https://doi.org/10.1016/j.addma.2016.05.007.

[21] H.Y. Wan, Z.J. Zhou, C.P. Li, G.F. Chen, G.P. Zhang, Effect of scanning strategy on grain structure and crystallographic texture of Inconel 718 processed by selective laser melting, J. Mater. Sci. Technol. 34 (2018) 1799–1804, https://doi.org/10.1016/j.jmst.2018.02.002.

[22] M. Calandri, S. Yin, B. Aldwell, F. Calignano, R. Lupoi, D. Ugues, Texture and microstructural features at different length scales in Inconel 718 produced by selective laser melting, in: Materials, 12, Basel,, 2019, https://doi.org/10.3390/ma12081293.

[23] D. Du, A. Dong, D. Shu, G. Zhu, B. Sun, X. Li, E. Lavernia, Influence of build orientation on microstructure, mechanical and corrosion behavior of Inconel 718 processed by selective laser melting, Mater. Sci. Eng. A. 760 (2019) 469–480, https://doi.org/10.1016/j.msea.2019.05.013.

[24] P. Karimi, E. Sadeghi, D. Deng, H. Gruber, J. Andersson, P. Nylén, Influence of build layout and orientation on microstructural characteristics of electron beam melted Alloy 718, Int. J. Adv. Manuf. Technol. 99 (2018) 2903–2913, https://doi.org/10.1007/s00170-018-2621-6.

[25] H. Yang, J. Yang, W. Huang, Z. Wang, X. Zeng, The printability, microstructure, crystallographic features and microhardness of selective laser melted Inconel 718 thin wall, Mater. Des. 156 (2018) 407–418, https://doi.org/10.1016/j.matdes.2018.07.007.

[26] T. Trosch, J. Strößner, R. Völkl, U. Glatzel, Microstructure and mechanical properties of selective laser melted Inconel 718 compared to forging and casting, Mater. Lett. 164 (2016) 428–431, https://doi.org/10.1016/j.matlet.2015.10.136.

[27] X. Wang, K. Chou, Effects of thermal cycles on the microstructure evolution of Inconel 718 during selective laser melting process, Addit, Manuf 18 (2017) 1–14, https://doi.org/10.1016/j.addma.2017.08.016.

[28] R.G. Ding, Z.W. Huang, H.Y. Li, I. Mitchell, G. Baxter, P. Bowen, Electron microscopy study of direct laser deposited IN718, Mater. Charact. 106 (2015) 324–337, https://doi.org/10.1016/j.matchar.2015.06.017.

[29] Q. Yu, C. Wang, Z. Zhao, C. Dong, Y. Zhang, New Ni-based superalloys designed for laser additive manufacturing, J. Alloy. Compd. 861 (2021), 157979, https://doi.org/10.1016/j.jallcom.2020.157979.

[30] W. Huang, J. Yang, H. Yang, G. Jing, Z. Wang, X. Zeng, Heat treatment of Inconel 718 produced by selective laser melting: Microstructure and mechanical properties, Mater. Sci. Eng. A 750 (2019) 98–107, https://doi.org/10.1016/j.msea.2019.02.046.

[31] Y. Zhao, K. Guan, Z. Yang, Z. Hu, Z. Qian, H. Wang, Z. Ma, The effect of subsequent heat treatment on the evolution behavior of second phase particles and mechanical properties of the Inconel 718 superalloy manufactured by selective laser melting, Mater. Sci. Eng. A. 794 (2020), 139931, https://doi.org/10.1016/j.msea.2020.139931.

[32] R. Cozar, A. Pineau, Morphology of y′and y" precipitates and thermal stability of inconel 718 type alloys, Metall. Trans. 4 (1973) 47–59.

[33] M.J. Donachie, S.J. Donachie, Superalloys: a technical guide, ASM international, 2002.

[34] R. M, S. Koppoju, G. Telasang, R. Korla, P. G, Effect of solutionizing temperature on the microstructural evolution during double aging of powder bed fusion-additive manufactured IN718 alloy, Mater. Charact. 172 (2021), 110868, https://doi.org/10.1016/j.matchar.2020.110868.

[35] G.H. Cao, T.Y. Sun, C.H. Wang, X. Li, M. Liu, Z.X. Zhang, P.F. Hu, A.M. Russell, R. Schneider, D. Gerthsen, Z.J. Zhou, C.P. Li, G.F. Chen, Investigations of γ′ γ″ and δ precipitates in heat-treated Inconel 718 alloy fabricated by selective laser melting, Mater. Charact. 136 (2018) 398–406, https://doi.org/10.1016/j.matchar.2018.01.006.

[36] L. Zhou, A. Mehta, B. McWilliams, K. Cho, Y. Sohn, Microstructure, precipitates and mechanical properties of powder bed fused inconel 718 before and after heat treatment, J. Mater. Sci. Technol. 35 (2019) 1153–1164, https://doi.org/10.1016/j.jmst.2018.12.006.

[37] T.G. Gallmeyer, S. Moorthy, B.B. Kappes, M.J. Mills, B. Amin-Ahmadi, A. P. Stebner, Knowledge of process-structure-property relationships to engineer better heat treatments for laser powder bed fusion additive manufactured Inconel 718, Addit. Manuf. 31 (2020), 100977, https://doi.org/10.1016/j.addma.2019.100977.

[38] W.M. Tucho, P. Cuvillier, A. Sjolyst-Kverneland, V. Hansen, Microstructure and hardness studies of Inconel 718 manufactured by selective laser melting before and after solution heat treatment, Mater. Sci. Eng. A. 689 (2017) 220–232, https://doi.org/10.1016/j.msea.2017.02.062.

[39] J. Li, Z. Zhao, P. Bai, H. Qu, B. Liu, L. Li, L. Wu, R. Guan, H. Liu, Z. Guo, Microstructural evolution and mechanical properties of IN718 alloy fabricated by selective laser melting following different heat treatments, J. Alloy. Compd. 772 (2019) 861–870, https://doi.org/10.1016/j.jallcom.2018.09.200.

[40] B. Gault, M.P. Moody, J.M. Cairney, S.P. Ringer, Atom probe microscopy. & Business Media, Springer Science, 2012.

[41] S.A. Mantri, S. Dasari, A. Sharma, T. Alam, M.V. Pantawane, M. Pole, S. Sharma, N. B. Dahotre, R. Banerjee, S. Banerjee, Effect of micro-segregation of alloying elements on the precipitation behaviour in laser surface engineered Alloy 718, Acta Mater. 210 (2021), https://doi.org/10.1016/j.actamat.2021.116844.

[42] D.J. Larson, R.M. Ulfig, D.R. Lenz, J.H. Bunton, J.D. Shepard, T.R. Payne, K.P. Rice, Y. Chen, T.J. Prosa, D.J. Rauls, T.F. Kelly, N. Sridharan, S. Babu, Microstructural investigations in metals using atom probe tomography with a novel specimen-electrode geometry, Jom 70 (2018) 1776–1784, https://doi.org/10.1007/s11837-018-2982-1.

[43] C. Kumara, A.R. Balachandramurthi, S. Goel, F. Hanning, J. Moverare, Toward a better understanding of phase transformations in additive manufacturing of Alloy 718, Materialia 13 (2020), 100862, https://doi.org/10.1016/j.mtla.2020.100862.

[44] C. Kumara, D. Deng, F. Hanning, M. Raanes, J. Moverare, P. Nylén, Predicting the microstructural evolution of electron beam melting of alloy 718 with phase-field modeling, Metall. Mater. Trans. A Phys. Metall. Mater. Sci. 50 (2019) 2527–2537, https://doi.org/10.1007/s11661-019-05163-7.

[45] F. Zhang, L.E. Levine, A.J. Allen, M.R. Stoudt, G. Lindwall, E.A. Lass, M. E. Williams, Y. Idell, C.E. Campbell, Effect of heat treatment on the microstructural evolution of a nickel-based superalloy additive-manufactured by laser powder bed fusion, Acta Mater. 152 (2018) 200–214, https://doi.org/10.1016/j.actamat.2018.03.017.

[46] A. Piglione, B. Attard, V. Vieira Rielli, C.-T. Santos Maldonado, M.M. Attallah, S. Primig, M.-S. Pham, On the constitutive relationship between solidification cells and the fatigue behaviour of IN718 fabricated by laser powder bed fusion, Addit. Manuf. 47 (2021), 102347, https://doi.org/10.1016/j.addma.2021.102347.

[47] G.F. Vander Voort, Metallography, principles and practice, ASM international, Materials Park, OH (1999).

[48] D.P. Field, P.B. Trivedi, S.I. Wright, M. Kumar, Analysis of local orientation gradients in deformed single crystals, Ultramicroscopy 103 (2005) 33–39, https://doi.org/10.1016/j.ultramic.2004.11.016.

[49] F. Theska, S.P. Ringer, S. Primig, Atom probe microscopy of strengthening effects in alloy 718, Microsc. Micro 25 (2019) 470–480, https://doi.org/10.1017/S1431927618015611.

[50] R. Cunningham, C. Zhao, N. Parab, C. Kantzos, J. Pauza, K. Fezzaa, T. Sun, A. D. Rollett, Keyhole threshold and morphology in laser melting revealed by ultrahigh-speed x-ray imaging, Sci. (80-.) 363 (2019) 849 LP–849852, https://doi.org/10.1126/science.aav4687.

[51] H.L. Wei, J. Mazumder, T. DebRoy, Evolution of solidification texture during additive manufacturing, Sci. Rep. 5 (2015) 1–7, https://doi.org/10.1038/srep16446.

[52] M.-S. Pham, B. Dovgyy, P.A. Hooper, C.M. Gourlay, A. Piglione, The role of side-branching in microstructure development in laser powder-bed fusion, Nat. Commun. 11 (2020) 749, https://doi.org/10.1038/s41467-020-14453-3.

[53] T. Voisin, J.B. Forien, A. Perron, S. Aubry, N. Bertin, A. Samanta, A. Baker, Y. M. Wang, New insights on cellular structures strengthening mechanisms and thermal stability of an austenitic stainless steel fabricated by laser powder-bed-fusion, Acta Mater. 203 (2021), https://doi.org/10.1016/j.actamat.2020.11.018.

[54] Y. Cao, P. Bai, F. Liu, X. Hou, Investigation on the precipitates of IN718 alloy fabricated by selective laser melting, in: Metals, 9, Basel,, 2019, pp. 1–10, https://doi.org/10.3390/met9101128.

[55] Y. Wang, J. Shi, Y. Liu, Competitive grain growth and dendrite morphology evolution in selective laser melting of Inconel 718 superalloy, J. Cryst. Growth 521 (2019) 15–29, https://doi.org/10.1016/j.jcrysgro.2019.05.027.

[56] P. Tao, H. Li, B. Huang, Q. Hu, S. Gong, Q. Xu, The crystal growth, intercellular spacing and microsegregation of selective laser melted Inconel 718 superalloy, Vacuum 159 (2019) 382–390, https://doi.org/10.1016/j.vacuum.2018.10.074.

[57] M.M. Attallah, R. Jennings, X. Wang, L.N. Carter, Additive manufacturing of Ni-based superalloys: the outstanding issues, MRS Bull. 41 (2016) 758–764, https://doi.org/10.1557/mrs.2016.211.

[58] S. Sanchez, P. Smith, Z. Xu, G. Gaspard, C.J. Hyde, W.W. Wits, I.A. Ashcroft, H. Chen, A.T. Clare, Powder bed fusion of nickel-based superalloys: a review, Int. J. Mach. Tools Manuf. 165 (2021), https://doi.org/10.1016/j.ijmachtools.2021.103729.

[59] V.V. Rielli, F. Theska, F. Godor, A. Stanojevic, B. Oberwinkler, S. Primig, Evolution of nanoscale precipitates during common Alloy 718 ageing treatments, Mater. Des. 205 (2021), 109762, https://doi.org/10.1016/j.matdes.2021.109762.

[60] M.K. Miller, J.A. Horton, W.D. Cao, R.L. Kennedy, Characterization of the effects of boron and phosphorus additions to the nickel-based superalloy 718, J. Phys. IV JP 6 (1996) 1–6, https://doi.org/10.1051/jp4:1996539.

[61] S.L. Lu, H.P. Tang, S.M.L. Nai, Y.Y. Sun, P. Wang, J. Wei, M. Qian, Intensified texture in selective electron beam melted Ti-6Al-4V thin plates by hot isostatic pressing and its fundamental influence on tensile fracture and properties, Mater. Charact. 152 (2019) 162–168, https://doi.org/10.1016/j.matchar.2019.04.019.

[62] R. Muñoz-Moreno, V.D. Divya, S.L. Driver, O.M.D.M. Messé, T. Illston, S. Baker, M. A. Carpenter, H.J. Stone, Effect of heat treatment on the microstructure, texture and elastic anisotropy of the nickel-based superalloy CM247LC processed by selective laser melting, Mater. Sci. Eng. A. 674 (2016) 529–539, https://doi.org/10.1016/j.msea.2016.06.075.

[63] X.Y. Fang, H.Q. Li, M. Wang, C. Li, Y.B. Guo, Characterization of texture and grain boundary character distributions of selective laser melted Inconel 625 alloy, Mater. Charact. 143 (2018) 182–190, https://doi.org/10.1016/j.matchar.2018.02.008.

[64] H.J. Lee, H.K. Kim, H.U. Hong, B.S. Lee, Influence of the focus offset on the defects, microstructure, and mechanical properties of an Inconel 718 superalloy fabricated by electron beam additive manufacturing, J. Alloy. Compd. 781 (2019) 842–856, https://doi.org/10.1016/j.jallcom.2018.12.070.

[65] F. Theska, A. Stanojevic, B. Oberwinkler, S.P. Ringer, S. Primig, On conventional versus direct ageing of Alloy 718, Acta Mater. 156 (2018) 116–124, https://doi.org/10.1016/j.actamat.2018.06.034.

[66] M.K. Miller, M.G. Hetherington, Local magnification effects in the atom probe, Surf. Sci. 246 (1991) 442–449, https://doi.org/10.1016/0039-6028(91)90449-3.

[67] M.P. Jackson, R.C. Reed, Heat treatment of UDIMET 720Li: the effect of microstructure on properties, Mater. Sci. Eng. A. 259 (1999) 85–97, https://doi.org/10.1016/S0921-5093(98)00867-3.

[68] F. Theska, A. Stanojevic, B. Oberwinkler, S. Primig, Microstructure-property relationships in directly aged Alloy 718 turbine disks, Mater. Sci. Eng. A. 776 (2020), 138967, https://doi.org/10.1016/j.msea.2020.138967.

[69] P. Promoppatum, S.-C. Yao, Influence of scanning length and energy input on residual stress reduction in metal additive manufacturing: numerical and experimental studies, J. Manuf. Process. 49 (2020) 247–259, https://doi.org/10.1016/j.jmapro.2019.11.020.

[70] E.R. Denlinger, V. Jagdale, G.V. Srinivasan, T. El-Wardany, P. Michaleris, Thermal modeling of inconel 718 processed with powder bed fusion and experimental validation using in situ measurements, Addit. Manuf. 11 (2016) 7–15, https://doi.org/10.1016/j.addma.2016.03.003.

[71] M.L. Griffith, M.T. Ensz, J.D. Puskar, C.V. Robino, J.A. Brooks, J.A. Philliber, J. E. Smugeresky, W.H. Hofmeister, Understanding the microstructure and properties of components fabricated by laser engineered net shaping (LENS), MRS online proc, Libr 625 (2000) 9, https://doi.org/10.1557/PROC-625-9.

[72] L. Liu, Q. Ding, Y. Zhong, J. Zou, J. Wu, Y.L. Chiu, J. Li, Z. Zhang, Q. Yu, Z. Shen, Dislocation network in additive manufactured steel breaks strength–ductility trade-off, Mater. Today 21 (2018) 354–361, https://doi.org/10.1016/j.mattod.2017.11.004.

[73] I. Serrano-Munoz, A. Ulbricht, T. Fritsch, T. Mishurova, A. Kromm, M. Hofmann, R. C. Wimpory, A. Evans, G. Bruno, Scanning manufacturing parameters determining the residual stress state in LPBF IN718 small parts, Adv. Eng. Mater. N./a (2021) 2100158, https://doi.org/10.1002/adem.202100158.

[74] V.D. Divya, R. Muñoz-Moreno, O.M.D.M. Messé, J.S. Barnard, S. Baker, T. Illston, H.J. Stone, Microstructure of selective laser melted CM247LC nickel-based superalloy and its evolution through heat treatment, Mater. Charact. 114 (2016) 62–74, https://doi.org/10.1016/j.matchar.2016.02.004.

[75] K.A. Jackson, J.D. Hunt, D.R. Uhlmann, T.P. Seward, On origin of equiaxed zone in castings, Trans. Metall. Soc. AIME 236 (1966) 149.

[76] R. Acharya, J.A. Sharon, A. Staroselsky, Prediction of microstructure in laser powder bed fusion process, Acta Mater. 124 (2017) 360–371, https://doi.org/10.1016/j.actamat.2016.11.018.

[77] B. Radhakrishnan, R.G. Thompson, A phase diagram approach to study liquation cracking in alloy 718, Metall. Trans. A 22 (1991) 887–902, https://doi.org/10.1007/BF02658999.

[78] G.A. Knorovsky, M.J. Cieslak, T.J. Headley, A.D. Romig, W.F. Hammetter, INCONEL 718: A solidification diagram, Metall. Trans. A. 20 (1989) 2149–2158, https://doi.org/10.1007/BF02650300.

[79] A. Drexler, B. Oberwinkler, S. Primig, C. Turk, E. Povoden-Karadeniz, A. Heinemann, W. Ecker, M. Stockinger, Experimental and numerical investigations of the γ'' and γ' precipitation kinetics in Alloy 718, Mater. Sci. Eng. A. 723 (2018) 314–323, https://doi.org/10.1016/j.msea.2018.03.013.

[80] D.D. Krueger, Dev. Direct Age 718 Gas. Turbine Engine Disk Appl. (2012) 279–296, https://doi.org/10.7449/1989/superalloys_1989_279_296.

[81] J.F. Radavich, Phys. Metall. Cast. Wrought Alloy 718 (2012) 229–240, https://doi.org/10.7449/1989/superalloys_1989_229_240.

[82] J. Schneider, B. Lund, M. Fullen, Effect of heat treatment variations on the mechanical properties of Inconel 718 selective laser melted specimens, Addit. Manuf. 21 (2018) 248–254, https://doi.org/10.1016/j.addma.2018.03.005.

[83] F. Liu, X. Lin, G. Yang, M. Song, J. Chen, W. Huang, Microstructure and residual stress of laser rapid formed Inconel 718 nickel-base superalloy, Opt. Laser Technol. 43 (2011) 208–213, https://doi.org/10.1016/j.optlastec.2010.06.015.

[84] J. Cao, F. Liu, X. Lin, C. Huang, J. Chen, W. Huang, Effect of overlap rate on recrystallization behaviors of Laser Solid Formed Inconel 718 superalloy, Opt. Laser Technol. 45 (2013) 228–235, https://doi.org/10.1016/j.optlastec.2012.06.043.

[85] R.C. Reed, The Superalloys: Fundamentals And Applications, Cambridge university press, 2008.

[86] Y. Zhao, K. Li, M. Gargani, W. Xiong, A comparative analysis of Inconel 718 made by additive manufacturing and suction casting: Microstructure evolution in homogenization, Addit. Manuf. 36 (2020), 101404, https://doi.org/10.1016/j.addma.2020.101404.

[87] V.V. Rielli, F. Theska, S. Primig, Correlative approach for atom probe sample preparation of interfaces using plasma focused ion beam without lift-out, Microsc. Microanal. (2021) 1–11, https://doi.org/10.1017/S1431927621000349.
[88] S. Zhang, X. Lin, L. Wang, X. Yu, Y. Hu, H. Yang, L. Lei, W. Huang, Strengthening mechanisms in selective laser-melted Inconel718 superalloy, Mater. Sci. Eng. A. 812 (2021), 141145, https://doi.org/10.1016/j.msea.2021.141145.
[89] H. Yang, J. Yang, W. Huang, G. Jing, Z. Wang, X. Zeng, Controllable in-situ aging during selective laser melting: stepwise precipitation of multiple strengthening phases in Inconel 718 alloy, J. Mater. Sci. Technol. 35 (2019) 1925–1930, https://doi.org/10.1016/j.jmst.2019.05.024.
[90] F. Theska, K. Nomoto, F. Godor, B. Oberwinkler, A. Stanojevic, S.P. Ringer, S. Primig, On the early stages of precipitation during direct ageing of Alloy 718, Acta Mater. 188 (2020) 492–503, https://doi.org/10.1016/j.actamat.2020.02.034.
[91] I. Kirman, D.H. Warrington, The precipitation of Ni3Nb phases in a Ni-Fe-Cr-Nb alloy, Metall. Trans. 1 (1970) 2667–2675, https://doi.org/10.1007/BF03037800.
[92] X. Gong, W.W. Xu, C. Cui, Q. Yu, W. Wang, T. Gang, L. Chen, Exploring alloying effect on phase stability and mechanical properties ofγ''-Ni3Nb precipitates with first-principles calculations, Mater. Des. 196 (2020), 109174, https://doi.org/10.1016/j.matdes.2020.109174.
[93] M. Bäker, J. Rösler, Influence of transition group elements on the stability of the γ''-phase in nickelbase alloys, Model. Simul. Mater. Sci. Eng. 29 (2021), https://doi.org/10.1088/1361-651X/abd043.
[94] M. Sundararaman, P. Mukhopadhyay, S. Banerjee, Some aspects of the precipitation of metastable intermetallic phases in INCONEL 718, Metall. Trans. A. 23 (1992) 2015–2028, https://doi.org/10.1007/BF02647549.
[95] F. Zhang, W. Cao, C. Zhang, S. Chen, J. Zhu, D. Lv, Simulation of co-precipitation kinetics of γ' and γ'' in superalloy 718, Springe Int. Publ. (2018), https://doi.org/10.1007/978-3-319-89480-5_8.
[96] A.J. Goodfellow, Strengthening mechanisms in polycrystalline nickel-based superalloys, Mater. Sci. Technol. (U. Kingd.). 34 (2018) 1793–1808, https://doi.org/10.1080/02670836.2018.1461594.
[97] T. Osada, Y. Gu, N. Nagashima, Y. Yuan, T. Yokokawa, H. Harada, Optimum microstructure combination for maximizing tensile strength in a polycrystalline superalloy with a two-phase structure, Acta Mater. 61 (2013) 1820–1829, https://doi.org/10.1016/j.actamat.2012.12.004.